

Advances in lithium niobate thin-film lasers and amplifiers: a review

Qiang Luo¹, Fang Bo,^{*} Yongfa Kong, Guoquan Zhang¹, and Jingjun Xu

Nankai University, TEDA Institute of Applied Physics and School of Physics, MOE Key Laboratory of Weak-Light Nonlinear Photonics, Tianjin, China

Abstract. Lithium niobate (LN) thin film has received much attention as an integrated photonic platform, due to its rich and great photoelectric characteristics, based on which various functional photonic devices, such as electro-optic modulators and nonlinear wavelength converters, have been demonstrated with impressive performance. As an important part of the integrated photonic system, the long-awaited laser and amplifier on the LN thin-film platform have made a series of breakthroughs and important progress recently. In this review paper, the research progress of lasers and amplifiers realized on lithium niobate thin film platforms is reviewed comprehensively. Specifically, the research progress on optically pumped lasers and amplifiers based on rare-earth ions doping of LN thin films is introduced. Some important parameters and existing limitations of the current development are discussed. In addition, the implementation scheme and research progress of electrically pumped lasers and amplifiers on LN thin-film platforms are summarized. The advantages and disadvantages of optically and electrically pumped LN thin film light sources are analyzed. Finally, the applications of LN thin film lasers and amplifiers and other on-chip functional devices are envisaged.

Keywords: integrated photonics; lithium niobate thin film; microlasers; amplifiers.

Received Dec. 10, 2022; revised manuscript received Apr. 11, 2023; accepted for publication Apr. 26, 2023; published online May 30, 2023.

© The Authors. Published by SPIE and CLP under a Creative Commons Attribution 4.0 International License. Distribution or reproduction of this work in whole or in part requires full attribution of the original publication, including its DOI.

[DOI: [10.1117/1.AP.5.3.034002](https://doi.org/10.1117/1.AP.5.3.034002)]

1 Introduction

Lithium niobate (LN) has rich physical effects, such as electro-optic, nonlinear, photorefractive, piezoelectric, pyroelectric, and wide transparent window (0.35 to 5 μm) and therefore has attracted extensive attention since the 1960s. In the early stages, the research on integrated LN photonic devices was mainly based on the titanium-diffusion or proton-exchange LN waveguides. These waveguides have large mode sizes ($\sim 10 \mu\text{m}$) and weak refractive index contrast (~ 0.1) limiting the performance of integrated devices and the development of large-scale integration. Fortunately, LN on insulator (LNOI) prepared by the smart-cut process has been successfully developed in the past two decades, which makes optical waveguides based on LNOI have small mode sizes ($\sim 1 \mu\text{m}^2$) and high refractive index contrast (~ 0.7) revolutionizing the research on integrated photonics.¹⁻³ Recently, micro-nano fabrication processes such as electron beam lithography-argon ion beam etching (EBL-Ar⁺

etching)⁴ and photolithography-assisted chemo-mechanical etching (PLACE)⁵, as well as ultraviolet lithography (UVL)-Ar⁺ etching⁶ have been developed. Microcavities based on an LNOI platform with high quality factor (10^7 to 10^8)^{7,8} and waveguide with low transmission loss (0.027 dB/cm)^{9,10} have been successfully demonstrated. In addition, due to the excellent electro-optic coefficient of LN and the strong mode field overlap between the electric field and optical mode rendered by the LNOI platform, electro-optic modulators operating with CMOS-compatible driving voltages and 3-dB bandwidths up to 100 GHz were realized on LNOI.^{11,12} The overall performance is exceeding or comparable with the counterpart based on other mature integrated photonics platforms.^{13,14} Meanwhile, efficient periodically polarized lithium niobate (PPLN) wavelength converters¹⁵⁻¹⁸ and optical frequency combs¹⁹⁻²¹ have also been demonstrated on this platform. With the tremendous advance in LNOI passive devices and applications, LNOI-based photonics is regarded as an ideal platform for realizing multifunctional integrated photonic circuits.²²⁻²⁶

On the other hand, active optical devices, such as lasers and amplifiers, on the LNOI platform have also been expected for

*Address all correspondence to Fang Bo, bofang@nankai.edu.cn

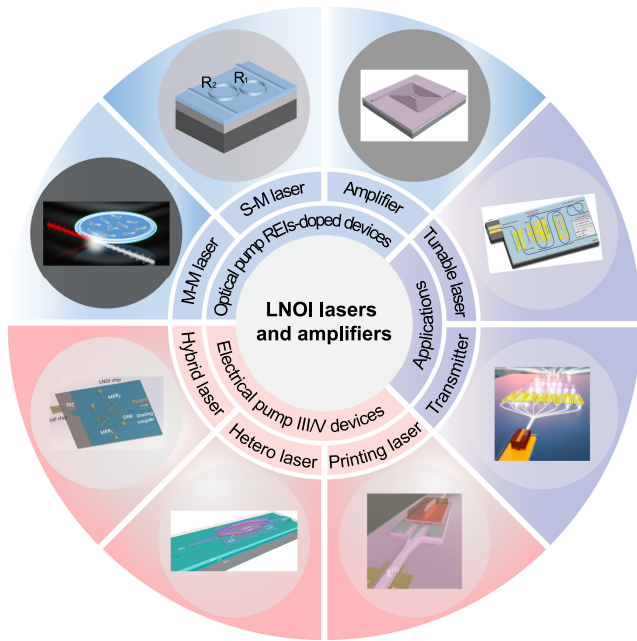


Fig. 1 Research field overview of LNOI light sources and amplifiers, which can be roughly classified into three parts: the optical-pump REI-doped devices and electrical-pump III/V devices and their applications. Some schematic sources: M-M (multi-mode) laser, reprinted from Ref. 27; S-M (single-mode) laser, reprinted from Ref. 28; amplifier, reprinted from Ref. 29; Hybrid laser, reprinted from Ref. 30, © 2021 Optica; hetero laser, reprinted from Ref. 31, © 2021 Optica; printing laser, reprinted from Ref. 32, © 2021 Optica; transmitter, reprinted from Ref. 33, © 2021 Optica; tunable laser, reprinted from Ref. 34 under a CC-BY license.

a long time as an essential part of integrated photonics. Due to the inherent indirect bandgap structure, it is difficult for LN to achieve electroluminescence. A simple and feasible scheme is to dope rare-earth ions (REIs) into LN as a gain medium to realize light sources and amplifiers under an optical pump. In addition, lasers and amplifiers for LNOI integrated photonics can also be realized by hybrid integration of the commercial semiconductor lasers or amplifiers or heterogeneous integration of the III-V gain materials with an electrical pumping scheme.

This paper reviews the recent research on lasers and amplifiers developed on the LNOI platform. Figure 1 shows the research road map for the LNOI light sources and amplifiers, which is also the overall idea of this paper. In Sec. 2, the research processes of lasers and amplifiers based on REI doping LN are introduced. Specifically, the common methods of REI doping in LN crystals and the study of spectral characteristics of doped crystals are discussed first. Subsequently, the important parameters for characterizing microlasers are discussed. Then, the research works of multimode microdisk lasers, multimode microring lasers, single-mode lasers, and amplifiers on the REI-doped LN thin film are presented. At the same time, the challenges of laser and amplifier performance and the potential improvement scheme for the REI-doped LNOI lasers and amplifiers are discussed. In Sec. 3, the electrically pumped III-V lasers and amplifiers on LNOI platform, as well as the applications of the laser transmitter and tunable Pockels laser confirmed by deploying the electro-optical effect of LN are introduced. Then, the advantages and challenges of the LNOI III-V lasers

are analyzed with a comparison with REIs-doped lasers. In Sec. 4, the application prospects of LNOI-based lasers and amplifiers are explored, combined with other LNOI functional devices, such as sensing, broadband optical communication, and frequency converter. Finally, in Sec. 5, the contents of the whole review are briefly summarized. At the same time, future research and development of LNOI-based lasers and amplifiers are envisaged.

2 Optically Pumped Lasers and Amplifiers

The indirect bandgap structure of LN crystal makes it challenging to realize electrically pumped luminescence. Nevertheless, photoluminescence based on REI doping is a simple and effective method that is widely favored by researchers. For example, various REI-doped waveguide lasers and amplifiers based on bulk LN crystal have been confirmed successfully.^{35–38} Combined with the advantages of strong mode localization and low transmission loss, active devices based on REI-doped LNOI platforms are expected to achieve better performance. In this section, the recent progress of REIs doping, spectroscopic analysis, microlasers, as well as amplifiers based on REIs-doped LNOI platforms is summarized.

2.1 Rare-Earth Ion Doping and Spectroscopic Analysis

Roughly, there are three main ways to dope REIs into LN crystal. The first one is to add REI oxide for doping when growing LN crystal by the Czochralski method and obtain LN single crystal with uniform ion concentration,^{39,40} as shown in Figs. 2(a) and 2(d). The second method is thermal diffusion, mainly through vacuum deposition of the REI layer, and then selective doping through high-temperature diffusion,³⁷ as shown in Fig. 2(b). In thermal diffusion doping, the diffusion depth of REIs has the characteristics of from complementary error function (erfc)-like to semi-Gaussian shape distribution [Fig. 2(e)].⁴¹ Due to the low diffusion rate of REIs, the diffusion temperature must be close to the Curie temperature of LN, which is generally as high as 1100°C and requires a diffusion time of up to 150 h. The diffusion time depends on the crystal phase of the LN substrate. The third method is to dope LN crystals with REIs by ion implantation,⁴² as shown in Fig. 2(c). At room temperature, ions are accelerated to million electron volt energy by Van der Graaff accelerator or transistor accelerator and implanted into the LN crystal. The ion concentration displays a nearly Gaussian distribution [Fig. 2(f)] and high-temperature annealing above 1000°C is needed to eliminate the defects caused by implantation and restore the quality of single-crystal LN.

The above three doping methods are relatively mature technologies after a long time of development and are expected to realize industrialization. But they also have their advantages and disadvantages. For example, compared to diffusion and ion implantation doping, crystal growth doping can obtain a high doping concentration and more uniform ion distribution and thus has a promising future in realizing high power and low transmission loss lasers and amplifiers. In contrast, for thermal diffusion and ion implantation, the maximum concentration of doped erbium ions is ~0.5%⁴³ and ~0.20% (molar fractions; hereinafter percentages referring to doping concentrations represent molar fractions, unless specified otherwise),⁴⁴ respectively, and the distribution of ions is erfc-like or Gaussian distribution, which has certain restrictions on the development of applications with high doping concentration, such as

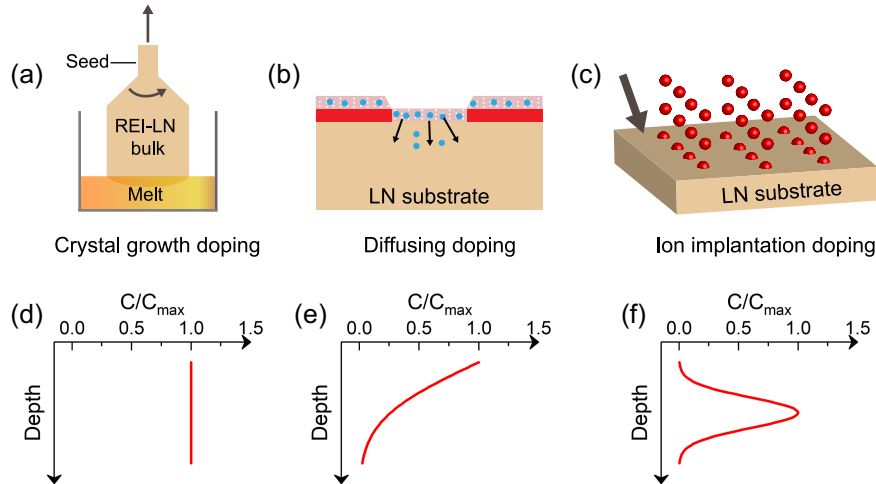


Fig. 2 Methods for REI doping into LN crystal and the corresponding concentration-depth distribution. (a) and (d) Crystal growth doping; (b) and (e) thermal diffusing doping; and (c) and (f) ion implantation doping. C , doping concentration and C_{\max} , the available maximum doping concentration for the corresponding method.

amplifiers. However, it has the ability of local doping for thermal diffusion and ion implantation doping, so it can flexibly control the doping region and avoid additional loss of passive devices on integrated optical chips and becomes an ideal scheme to build a locally doped optical gain chip.

In recent years, referring to the incorporation of REIs into LN bulk crystal, many research groups have carried out research on REI-doped LNOI integrated photonics.^{45,46} For example, Dutta et al. first prepared 300-nm-thick thin-film LN from 0.1% thulium-doped X-cut LN bulk by the smart-cut process, and then prepared the grating coupling structure and single-mode waveguide by EBL-dry etching process, as shown in Fig. 3(a).⁴⁷ To explore the optical properties of thulium ions in the thin-film waveguide, the absorption, emission spectra, and fluorescence lifetime were measured at a 3.6 K low temperature. Compared to a thulium doped-bulk crystal, the thulium ions in smart-cut thin film displayed virtually identical optical properties, which indicates that the smart-cut process can preserve the optical properties of REIs in thin films well. Notably, the preparation of the REI-doped LNOI is compatible with wafer-scale integration, paving the way to achieve on-chip active photonics systems and applications. Furthermore, an atomic frequency comb memory was realized in thulium-doped LNOI waveguides by the same doping and fabrication process, and the storage spectrum bandwidth and optical storage time were up to 100 MHz and 250 ns, respectively.⁵³

Recently, Wang et al. explored the optical coherence of the erbium-doped smart-cut LN thin film prepared from bulk erbium-doped LN. Experimentally, 180- μ s optical coherence time was obtained by fitting the exponential decay curve of the echo signal strength as a function of time delay.⁵⁴ The coherence time, also referring to coherence lifetime, is a parameter to reflect the homogeneous broadening linewidth of the REI spectrum and thus indicates the ability of application for quantum information processing.^{55,56} The obtained coherence time is comparable with the value of bulk crystal, indicating that the erbium-doped smart-cut LN thin-film platform shows promise for developing on-chip quantum storage. At the same time, Rüter et al. characterized the spectral properties of a neodymium-doped LN

thin film fabricated from an LN substrate diffusion-doped with neodymium ions before the smart-cut fabrication process and showed an opportunity to realize active gain areas with locally varying doping concentrations.⁵⁷

In addition, Wang et al. also carried out research on ion implantation doping based on a prepared LNOI microcavity. First, a microring coupled with a waveguide was fabricated by the EBL-Ar⁺ etching process. Then, erbium ions were doped by ion implantation with an implantation energy of 350 keV and a flux fluence of 1.14×10^{14} ions/cm².⁴⁸ The optical properties could be partially recovered and the average Q value of the microring cavity is 5×10^5 after post-implantation annealing at 550°C for 5 h. The scanning electron microscope (SEM) image of the fabricated devices and the simulated ion density distribution are shown in Fig. 3(b). The fluorescence lifetime of erbium ion, defined as the time constant corresponding to the exponential decay of the ion from the energy level in the form of spontaneous emission or non-radiation reflecting the local environment of the ion, is measured as 3.2 ms at low temperatures. Such a fluorescence lifetime is higher than 2 ms in LN bulk crystal. Therefore, it reflects that there may be differences in the local environment of erbium ions, refractive index, and Li/Nb ratio of the material compared with the doped bulk LN.⁴² At the same time, the resonance-enhanced fluorescence decay caused by the coupling between ions and cavity was observed, which is referred to as the Purcell effect^{58,59} and is expected to develop high-efficiency light emitters.⁶⁰ The enhance factor is defined as the Purcell factor and can be expressed as $3Q\lambda^3/4\pi^2V$, where Q and V are the quality factor and mode volume of microcavity resonance mode, respectively.⁵⁹ In this work, the average Purcell factor was calculated as 3.8. In the same period, Pak et al. adopted a similar method to incorporate ytterbium ions into fabricated LNOI microring resonators and centimeter-long waveguides.⁴⁹ Figure 3(c) shows the schematic diagram of the ytterbium-doped LNOI waveguide structure and the simulation of implanted ytterbium ions distribution with a peak concentration of 0.0002%. The doped device was annealed at 500°C for 8 h under a nitrogen atmosphere to heal the lattice damage caused by ion implantation. The loaded Q of the microring

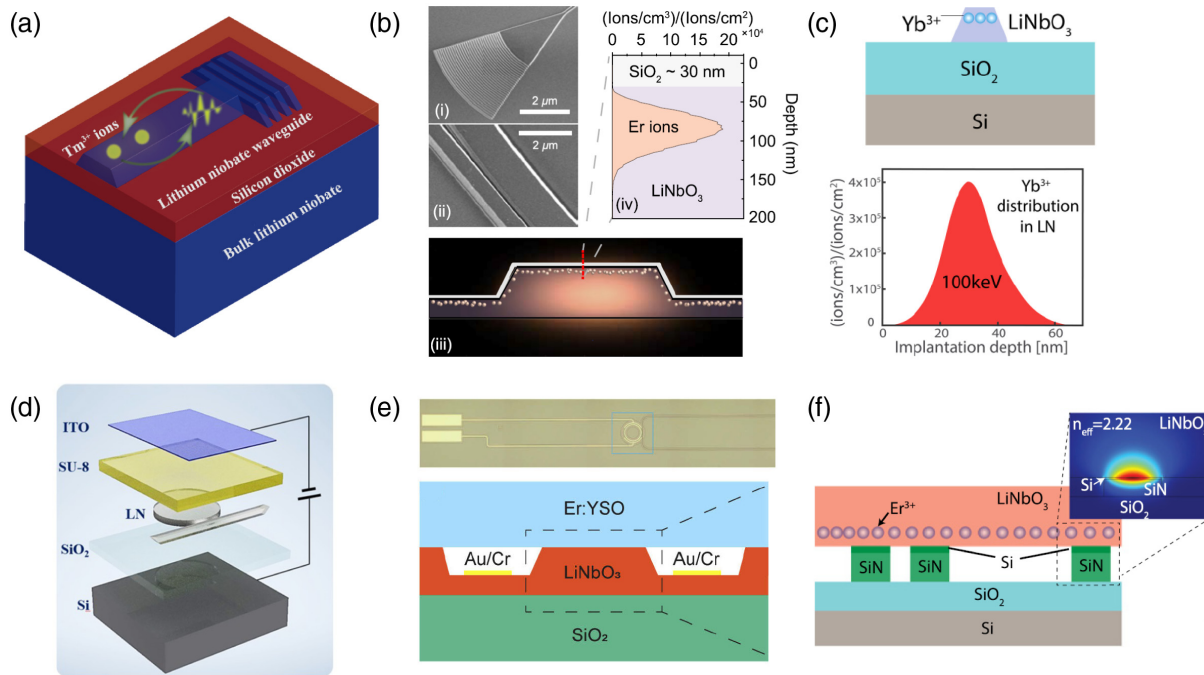


Fig. 3 (a) Schematic of the thulium-doped LNOI waveguide with grating couplers. Reprinted with permission from Ref. 47, © 2020 American Chemical Society. (b) SEM image and concentration distribution of erbium ions implanted in LNOI structure. Reprinted from Ref. 48, with the permission of AIP Publishing. (c) Schematic cross-sectional diagram and SRIM simulation distribution of ytterbium ions implanted in LNOI structure. Reprinted from Ref. 49, with the permission of AIP Publishing. (d) Schematic diagram of ytterbium ions implanted in LNOI tunable microcavities. Reprinted from Ref. 50, © 2022 Optica. (e) Optical micrograph of the LNOI device and schematic cross-sectional drawing after bonding with $\text{Er}^{3+}:\text{Y}_2\text{SiO}_5$. Reprinted from Ref. 51, © 2021 Optica. (f) Schematic cross-sectional view of the $\text{Er}:\text{LN}$ crystal integrated with Si-SiN waveguides and resonators. Reprinted from Ref. 52, with the permission of AIP Publishing.

was measured at 2×10^5 at 908 nm. The photoluminescence characterization found that the lifetime of ytterbium ions on resonator pumping is shortened slightly compared to nonresonant pumping, which is attributed to the Purcell-enhanced emission with a Purcell factor of 0.45.

At the same time, Xia et al. directly doped ytterbium ions into an X-cut LN thin film with a thickness of 470 nm by ion implantation.⁵⁰ After post-annealing at a slightly higher temperature of 650°C, no apparent film damage was observed. Then, ytterbium-doped microcavities with a radius of 7 μm and a Q of $\sim 2.4 \times 10^5$ were fabricated by EBL and chemical-mechanical etching protocol. A layer of indium tin oxide was deposited on the microcavity as an electrode to tune its resonant frequency electrically. The device schematic is shown in Fig. 3(d). Due to the ions-cavity coupling, the shortening of ytterbium ions' lifetime was demonstrated with a Purcell factor of 10.24. The coupling between the REIs and microcavity based on electro-optic tuning can be controlled at 5 μs switching speed over a 160 GHz range. In addition, the detection of a single ytterbium ion was carried out based on electro-optic dynamic tuning, which provides a platform for generating a deterministic single-photon source.

In addition, Yang et al. hybrid integrated the erbium-doped yttrium orthosilicate with a concentration of 50 ppm (parts per million) to LNOI microring by flip-chip bonding, as shown in Fig. 3(e).⁵¹ The fluorescence lifetime of erbium ions was measured as 11.5 ms, consistent with the bulk material result of 11.4 ms. At the same time, the resonance broadening phenomenon caused

by ion-cavity coupling was also observed, and the coupling intensity factor was assessed to be 0.36. Moreover, the erbium ions-implanted LN crystal directly integrated on a silicon photonic chip was reported by Jiang et al., as shown in Fig. 3(f). The optical properties of erbium ions in the integrated structure were investigated, and a modification of the photoluminescent emission was observed.⁵²

Affected by the differential thermal expansion rates of the layers in the LNOI wafer, the tolerable annealing temperature ($\sim 500^\circ\text{C}$) of the LNOI wafer is far below the required temperature of $\sim 1100^\circ\text{C}$ for the thermal-diffusion and ion-implantation doping of REIs into LN bulk crystal. Therefore, the incorporation of REIs into the LNOI platform by ion implantation methods after the smart-cut process significantly limited the doping concentration and ion distribution and naturally limited the optical properties of REIs. Fortunately, incorporating REIs into the LNOI platform before the smart-cut process is feasible. Additionally, this method can preserve the desirable optical properties in bulk crystals and can be compatible with scalable planar fabrication. Xu et al. studied the refractive index, erbium ion spectrum, and other material properties of the erbium-doped LN film prepared based on the smart-cut process. They found that the material properties of the LN film are close to the erbium-doped bulk LN. This indicates that high-quality REIs-doped LN film can be obtained based on the smart-cut process.⁶¹ This provides a path for the realization of on-chip LNOI lasers and amplifiers by adjusting an appropriate doping

concentration of the LN bulk sliced to a thin film. Thus, a series of groups have recently focused on realizing LNOI lasers and amplifiers based on REI-doped LN thin film.

2.2 Whispering Gallery Microcavity Lasers Based on REI-Doped LNOI

The three elements of a laser are the pump source, the gain medium, and the resonator. The gain medium and pump wavelength are determined by selecting the type of REI. The resonant cavity of a traditional laser is mainly composed of two or more mirrors. Compared with traditional resonators, whispering gallery mode (WGM) microcavities with circular structures can confine light by “continuous total internal reflection” for a long time within an ultrasmall mode volume, leading to strong light–matter interactions. Benefiting from the high quality factor (Q) and small mode volume (V), WGM microcavity is regarded as an ideal platform to realize ultralow threshold lasers with a small footprint and narrow linewidth.^{62–64} For example, Yang et al. reported an erbium-doped microlaser on a silicon chip with an ultralow threshold of 660 nW.⁶⁵ In this section, some important parameters for the characterization of WGM lasers were first discussed in Sec. 2.2.1. Then the development status of multimode microdisk and microring lasers based on REI-doped LNOI was introduced in Sec. 2.2.2. Finally, the research progress of the single-mode lasers and development constraints for the REI-doped LNOI microlasers were analyzed in Sec. 2.2.3.

2.2.1 Important parameters for characterizing microlasers

Before introducing the research progress of microlasers based on REI-doped LNOI, we discuss some important parameters for characterizing microlaser performance.

Lasing threshold. The lasing threshold refers to the pump power when the gain provided by the gain medium is just equal to the loss of the laser cavity. The pump threshold power (P_{th}) of WGM microcavity laser can be approximately expressed as⁶⁶

$$P_{\text{th}} \approx \frac{2\pi n_1 h c V_p}{\lambda_1 \lambda_p Q_1 \eta \sigma_{\text{em}} \tau}, \quad (1)$$

where n_1 and Q_1 refer to the effective refractive index and quality factor of the corresponding laser signal mode, respectively. λ_1 and λ_p indicate the signal and pump wavelengths, respectively. V_p is the mode volume of the pump mode, and η is the pump efficiency. h and c refer to the Planck constant and the speed of light in vacuum, respectively. σ_{em} and τ respectively correspond to the stimulated emission cross section and fluorescence lifetime of the gain ions. As can be seen from Eq. (1), for a given gain medium, to obtain a low laser threshold, the effective way to reduce the laser threshold is to improve the pumping efficiency, increase the Q value of the resonator, and reduce the mode volume, which is also a significant advantage of conducting laser research based on WGM resonators. Specifically, high Q can be obtained by improving the processing technology. For example, the maximum Q value of an LNOI WGM cavity up to 10^8 has been demonstrated based on an ion-free preparation of LN thin film, which is close to the upper limit of the intrinsic absorption of bulk LN and shows great potential in the application of ultralow threshold lasers.⁶⁷ The mode volume can be reduced by reducing the size or thickness of the resonant cavity. However, it should be noted that too small

a diameter or thickness may lead to increased radiation loss of the resonant cavity, and the balance between the Q and V needs to be considered in the actual research to obtain a maximum value of Q/V . In addition, the optimization of pumping efficiency involves major factors such as the coupling between the tapered fiber (or waveguide) and the resonator, the overlap of the pump mode and signal mode in the gain medium, as well as the absorption of the gain medium to the pump.

Conversion efficiency and maximum laser output power. The conversion efficiency of a laser refers to the rate of change of the generated signal power relative to the pump power at the working stage above the lasing threshold, which reflects the conversion efficiency from the pump to signal during the laser operation. At the same time, it is obvious that the maximum laser output power refers to the maximum power that can be obtained when the laser is working, which can reflect the available power level of the laser for subsequent work. For optimizing these two parameters, laser signal extraction should also be optimized. That is to say, high pump efficiency and signal extraction efficiency should be guaranteed simultaneously. However, because the pump and signal are in different bands, the coupling state between a tapered fiber or straight waveguide and a resonator is inconsistent. Generally, the maximum output power of the laser is observed when the pump light is in an overcoupled regime in the experiment. To realize high conversion efficiency and low threshold, it is often necessary to design a broadband coupling to meet the requirements of efficient pump and signal extraction.⁶⁸ In addition, different from optimizing the laser threshold, a large resonator size or cavity length is required to improve the gain accumulation to obtain an intense laser output.

Laser linewidth. Laser linewidth usually refers to the full width at half-height of the signal mode in the laser spectrum, which is an important parameter reflecting the coherence and noise of the laser. According to the Haken–Lax–Scully formula, the linewidth of the emitted laser operating above the threshold can be expressed as⁶⁹

$$\delta\nu = \frac{\pi h \nu (\Delta\nu)^2}{P} = \frac{\pi h \nu^3}{P Q^2}, \quad (2)$$

where h is the Planck constant, ν and P are the emitted frequency and power of the laser, respectively, and $\Delta\nu$ is the linewidth of the cavity mode. Increasing the resonator’s quality factor and output power is an effective way to reduce the linewidth of the laser. The discussion of other factors affecting laser performance, such as doping concentration, can be found in the previous review on WGM microcavity lasers.⁶³ Then, the research progress of multimode microdisk lasers, multimode microring lasers, and single-mode microlasers based on REI doped-LNOI platform is introduced in the following sections.

2.2.2 Multimode microdisk and microring lasers

Wang et al. reported an erbium-doped LNOI laser based on a 200- μm -diameter microdisk fabricated on an erbium-doped chip with a doping concentration of 1% by the PLACE process.⁷⁰ The Q factor was measured to be 1.8×10^6 at 1563 nm by the scanning transmission spectrum method. The emitted laser signal at the 1560-nm band and the accompanying strong green-up conversion fluorescence were observed under the 976-nm laser pump, as shown in Fig. 4(a). The threshold

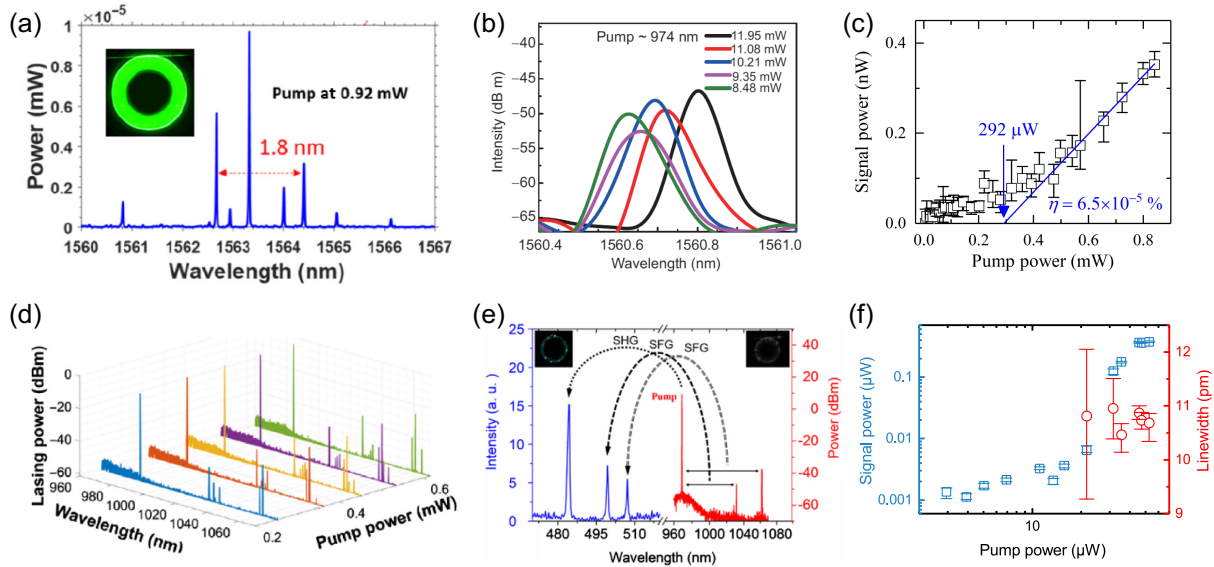


Fig. 4 (a) The emitted laser signal at the 1560-nm band under the 976 nm laser pump. Inset: the accompanied green-up conversion fluorescence. Reprinted from Ref. 70, © 2021 Optica. (b) The observed signal wavelength drift process with different pump powers for the 974 nm pump. Reprinted from Ref. 27. (c) The dependence of the dominant mode signal power on the pump power. Reprinted from Ref. 71. (d) The collected spectra at different pump power. (e) The observed SHG and SFG at the 969 nm laser pump. Inset, the captured photograph of the microdisk at the visible (left) and IR (right) regions. (d) and (e) Reprinted from Ref. 72, © 2021 Optica. (f) The dependence of signal power (squares) and linewidth (circles) of the dominating lasing mode on the increasing pump power. Reprinted from Ref. 73, © 2022 Optica.

of the laser signal was lower than $400 \mu\text{W}$, and the conversion efficiency was deduced as 1.92×10^{-4} by fitting the signal power data. In addition, the blue-shift (red-shift) of the signal wavelength at a lower (higher) pump power with a rate of -17.03 pm/mW (10.58 pm/mW) was observed. The possible reason for this shift process is that the photorefractive and thermo-optical effects of LN exist together, and the photorefractive effect is dominant at low pump power, while the thermo-optical effect dominates at high power.

Subsequently, Liu et al. fabricated a $150\text{-}\mu\text{m}$ -diameter microdisk by the focused ion milling process based on an erbium-doped LNOI wafer with a doping concentration of 1%.²⁷ The laser emission at 1550-nm band with a linewidth of $\sim 0.1 \text{ nm}$ was observed under the laser pumping at 974 and 1460 nm, respectively. Due to the thermal effect of the LN microdisk, the redshift processes of the emission signal wavelength were observed when increasing the pump power for both pump bands, and better thermal stability was obtained at a 1460-nm pump. The threshold for the 974-nm pump was measured as 2.99 mW with a conversion efficiency of 4.12×10^{-6} . At the same time, Luo et al. reported the batch preparation of erbium-doped LNOI microdisk lasers using UVL-Ar⁺ etching and an additional chemo-mechanical polishing (CMP) process.⁷¹ The threshold and conversion efficiency of the dominant signal mode in the 1530-nm band were deduced as $292 \mu\text{W}$ and 6.5×10^{-7} , respectively, as shown in Fig. 4(c).

Except for the 1550-nm band, the microlaser operating at other wavelength bands has many unique applications. For example, due to the negligible water absorption at the 1060-nm band, the ytterbium ion emission can be applied for biosensing. In addition, compared with an erbium ion, ytterbium ion has

a simple energy level structure and higher absorption cross section at the 980-nm band, which has substantial potential to improve the output power and conversion efficiency of micro-lasers. Zhou et al. first reported a microdisk laser based on a ytterbium-doped LNOI chip.⁷² With the continuous laser pump at 984 nm, the lasing signals at the 1030- and 1060-nm bands were observed in the increasing pump power range, as shown in Fig. 4(d). A threshold of $103 \mu\text{W}$ and a conversion efficiency of 0.53% for the collected signal laser were derived by linearly fitting the signal power data at the different pump powers. Compared to the erbium-doped LNOI microlaser, the conversion efficiency has been significantly improved due to the high quantum efficiency of ytterbium ions.^{74–76} Meanwhile, due to the strong nonlinearity of LN, the second-harmonic generation (SHG) of the pump laser and the sum frequency generation (SFG) between the pump and emission signal were also observed, as shown in Fig. 4(e).

Subsequently, Luo et al. also reported 1060-nm band microdisk lasers with a high conversion efficiency.⁷³ Based on an ytterbium-doped LNOI wafer with a doping concentration of 1.5%, the microdisk cavities were fabricated in a batch using UVL-Ar⁺ etching and the CMP process. The loaded Q factors at 970.20 and 1502.68 nm were measured as 5.56×10^4 and 4.0×10^6 , respectively. With a 980-nm band laser pump, the emission signal at the 1060-nm band was detected by OSA. The blueshift phenomenon of the signal mode wavelength at a $7.4 \text{ pm}/\mu\text{W}$ rate was observed under the increase of pump power due to the photorefractive effect of the LN crystal. The power and linewidth of the dominant signal mode under different pump powers are shown in Fig. 4(f). An S-shaped curve for the pump-power-dependent signal power was observed, which

indicates that the collected signal belongs to a lasing signal. The threshold and conversion efficiency were deduced as $21.19 \mu\text{W}$ and 1.36% , respectively. Benefiting from the high doping concentration and high Q factors of the fabricated microdisk, as well as the effective signal extraction, the conversion efficiency is the highest value for the reported REI-doped LNOI microlasers. This work significantly improved the microlaser performance and shows the potential of the LNOI platform in biosensing applications.

The research works of REI-doped LNOI laser described above are based on microdisk cavities. The microdisk cavity is mainly pumped and monitored by a fiber taper, which has the limitations of unstable coupling and inconvenient further integration with other on-chip functional devices. Microring cavities coupled with an on-chip waveguide can overcome these limitations. Furthermore, microring cavities usually have a smaller mode volume than a microdisk cavity with the same radius, which means that the light field power density in the cavity is more significant under the same pump power, leading to a lower laser threshold.

Luo et al. prepared a microring cavity coupled with a waveguide using the EBL- Ar^+ etching technique on a Z-cut erbium-doped LNOI wafer with a doping concentration of 0.1% .⁷⁷ The loaded Q at 1531.8 nm was measured as 4.27×10^5 (intrinsic $Q \sim 4.84 \times 10^5$), corresponding to a waveguide loss of 0.86 dB/cm . Under the 980-nm band continuous laser pump, lasing emission was realized in the 1530-nm band. The lasing threshold was estimated to be $\sim 20 \mu\text{W}$, and the conversion efficiency was deduced as 6.61×10^{-7} by linearly fitting the signal mode power data, as shown in Fig. 5(a). Benefiting from

the small mode volume and high optical power density of the microring structure, the achieved threshold is reduced by 1 order of magnitude compared with the erbium-doped microdisk laser. Till now, $20 \mu\text{W}$ is the lowest lasing threshold based on the reported REI-doped LNOI microlasers.

At the same time, Yin et al. fabricated a Z-cut erbium-doped LNOI microring cavity with 1% doping concentration and an undoped LNOI waveguide by the PLACE technique, respectively. Then, the LNOI microring was vertically coupled with the waveguide structure, as shown in the inset of Fig. 5(b).⁷⁸ With a 980-nm laser pump, a broadband lasing signal in the 1550-nm band was observed with different pump power. A lasing threshold of 3 mW was deduced by fitting the signal power data. The wavelength tuning of the mode around 1533 nm was electrically tuned in a range of 0.2 nm with an EO coefficient of 0.33 pm/V , as shown in Fig. 5(c), by applying an external voltage to the electrodes integrated with the racetrack microcavity.

In addition, an integrated ytterbium-doped LNOI microring laser working at 1060-nm band was recently demonstrated by Luo et al.⁷⁹ Similar to the reported erbium-doped microring laser,⁷⁷ the microring was fabricated using the EBL- Ar^+ etching technique on an ytterbium-doped LNOI wafer with a 1.5% doping concentration. In experiments, the multi-peaks in the range of 1056 to 1066 nm were observed when the pump wavelength tuned into the microring resonance mode, as shown in Fig. 5(d). The maximum signal power was up to $6.44 \mu\text{W}$ at 1060.49 nm , which is a great improvement compared with the previously reported erbium-doped LNOI microlaser. The signal power and linewidth of the dominant mode were recorded while increasing pump power, as shown in Fig. 5(e). By fitting the linear increase

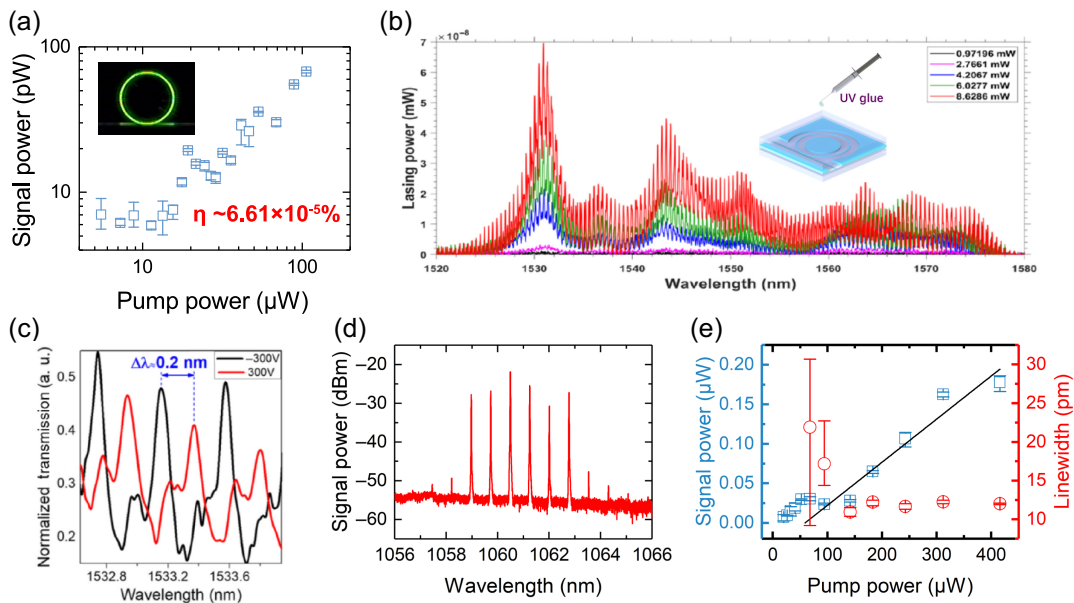


Fig. 5 (a) Collected power of signal mode under different pump powers. Inset: the captured green up-conversion fluorescence. Reprinted from Ref. 77, © 2021 Optica. (b) The detected emission spectra at different pump power. Inset: schematic of the bonding process for the microring and waveguide structures. (c) The recorded signal spectrum at 1533 nm for the varying electric voltage between -300 and $+300 \text{ V}$. (b) and (c) Reprinted from Ref. 78, © 2021 Optica. (d) Observed multi-peak signals at a pump power of $\sim 2.23 \text{ mW}$. (e) The signal power (blue square) and linewidth (red circle) of the dominant mode as a function of pump power. (d) and (e) Reprinted from Ref. 79, © 2022 Optica.

portion of signal power, the threshold and conversion efficiency were deduced as $59.32 \mu\text{W}$ and 5.45×10^{-4} , respectively. A higher conversion efficiency is expected to improve the pump efficiency and signal extraction efficiency by introducing the pulley waveguide coupling design. Due to the integrated feature and stable performance of microring cavities, these microring lasers may find more practical applications.

2.2.3 Single-mode lasers

Due to the broadband gain property of REIs, the REI-doped LNOI microcavity lasers introduced above generally operate in a multimode state, which is subject to false signals, random fluctuations, and instabilities and thus limits its application scenarios. Therefore, single-mode lasers featuring monochromaticity, high stability, and controllable output wavelength have attracted much attention due to their great potential for practical applications, such as optical communication and optical sensing. At present, there are four main ways to realize a single-mode laser. (1) Decreasing the size of the cavity to enlarge the free spectral range (FSR) and ensure only one resonant mode in the gain band range. (2) Designing narrowband distributed Bragg reflector (DBR) or distributed feedback (DFB) structures in the resonance cavity to achieve mode selection. (3) Cascading two or more cavities to realize mode selection by the Vernier effect. The specific mechanism is that the subcavities with different FSR (size) are coupled together. In such a system, the “supermode” is formed in the coupled cavities at the resonance overlapping location, while other normal modes resonate in only one cavity and dissipate in another cavity, resulting in greater

losses. Therefore, the supermode with enlarged FSR and higher Q values can be selected. Combined with the gain competition between the modes in the gain band, the single-mode operation of the laser can be realized. (4) Spatially selective pumping to suppress high-order mode gain or controlling mode loss to achieve single-mode lasing. Among them, reducing resonator size will increase the radiation loss of the light field in the cavity and thus increase the threshold power density of the laser, so this scheme is less commonly used. The following part will introduce the research progress of single-mode laser based on the REI-doped LNOI platform.

First, Gao et al. fabricated coupled microdisks, also referred to as photonic molecule, based on erbium-doped LNOI with 1% doping concentration using the PLACE technique.⁸⁰ The coupled microdisks with a diameter of 29.8 and 23.1 μm , respectively, are separated by a gap of 0.48 μm . Under the 977.7-nm laser pump, the single-mode laser emission at 1550.5 nm with a threshold of $\sim 200 \mu\text{W}$ was realized using the inverse Vernier effect, as shown in the spectra in Fig. 6(a). It is worth noting that the pump was resonant in both microdisks, and the signal was mainly localized in the small microdisk when the single-mode laser was working. In addition, a minimum signal linewidth of 348 kHz was characterized using a Michelson interferometer composed of an optical fiber coupler to measure the laser frequency and phase noise.

Subsequently, to effectively improve the integration and scalability of REI-doped LNOI single-mode lasers, Zhang et al. designed a microring photonic molecule with radii of 85 and 100 μm to achieve a single-mode laser, as shown in the inset

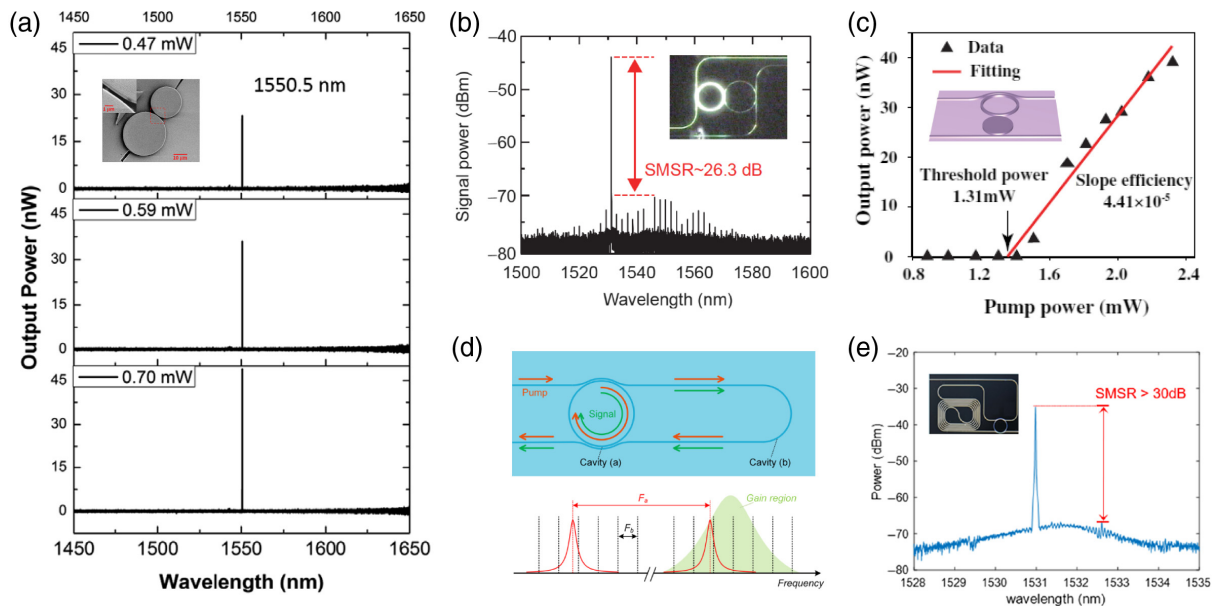


Fig. 6 (a) Single-mode lasing spectra at different pump power. Inset: SEM image of the fabricated coupled microdisks. Reprinted from Ref. 80, © 2021 Optica. (b) Single-mode lasing signal with a high SMSR in coupled microrings at a pump power of about 900 μW . Inset: the observed green up-conversion fluorescence in the photonic molecule. Reprinted from Ref. 28. (c) Single-mode laser power under different pump power. Inset: schematic diagram of the coupled microdisk and microring. Reprinted from Ref. 81, © 2021 Optica. (d) Schematic diagram of dual cavity laser and the operation principle of single-frequency laser. (e) Single frequency laser emission spectrum with an SMSR of 31 dB. Inset: the photograph of the designed dual cavity. (d) and (e) Reprinted from Ref. 82, © 2021 Optica.

of Fig. 6(b).²⁸ The photonic molecule was fabricated by the EBL-Ar⁺ etching process based on an X-cut erbium-doped LNOI chip with 0.1% doping concentration. In experiments, the double resonance at 1531.6 nm for the two microring cavities was confirmed by the transmission spectra. Moreover, the FSR of the supermodes of the photonic molecule was enlarged to 11 nm in the 1550-nm band due to the Vernier effect. At the same time, the nonsupermodes were also observed in the transmission spectrum, which have a lower coupling depth due to a greater loss and thus a higher lasing threshold. As a result, the single-mode laser was achieved in the supermodes. Figure 6(b) shows the collected emission signal spectra at a pump power of $\sim 900 \mu\text{W}$ showing a side-mode suppression ratio (SMSR) of up to 26.3 dB. The threshold was estimated as $\sim 200 \mu\text{W}$ by analyzing the signal power with the increasing pump power.

Soon afterward, to reduce the requirement of tunability of pump light, Liu et al. demonstrated an erbium-doped LNOI single-mode laser based on a photonic molecule with a microdisk and a microring, as shown in the inset of Fig. 6(c).⁸¹ In this device, a single-mode laser emission with an SMSR of 31.4 dB in the range of 1520 to 1570 nm was observed with a 974-nm LD light source pump. Figure 6(c) displays the collected single-mode laser power as a function of pump power. The threshold and slope efficiency were deduced as 1.31 mW and 4.41×10^{-5} , respectively. Moreover, the dependence of output power and wavelength on temperature was also investigated. With the increase in temperature, the output power increment and signal wavelength redshift were observed, which may be due to the change of cavity mode resonance state caused by the thermal-optic effect of LN.

During the same period, Xiao et al. designed a single-frequency erbium-doped LNOI laser based on a coupling structure composed of a short microring cavity with a diameter of 200 μm and a long cavity with a length of 1.2 cm.⁸² Figure 6(d) depicts the schematic diagram of coupling structure and the operation principle of single-frequency laser. The FSRs of the two cavities are $F_a \sim 200 \text{ GHz}$ and $F_b \sim 10 \text{ GHz}$, respectively. Based on the Vernier effect, only the frequency located in the gain bandwidth and resonated on both cavities can oscillate. With a 1484-nm laser pump, a single-frequency laser emission near 1531 nm with an SMSR of 31 dB was observed, as shown in Fig. 6(e). The linewidth of the obtained single-frequency laser was detected as 1.2 MHz through a self-heterodyne method. A threshold of 13.54 mW and a slope efficiency of 1.45×10^{-4} were measured as well. The reason for a relatively high threshold may be using a broadband source (0.5 nm) as the pump.

Actually, controlling mode loss is also a popular way to achieve single-mode lasing due to the compact device size. For example, Li et al. demonstrated a single-mode laser based on a single microring resonator by regulating the mode loss.⁸³ The microring resonator with a pulley waveguide was fabricated on a Z-cut 1% doped erbium-doped LNOI wafer using the EBL-Ar⁺ etching process. Based on simulation analysis, the supported four modes (TE_{00} , TE_{10} , TM_{00} , and TM_{10}) on the 2- μm -wide microring are shown in Fig. 7(a). Compared to mode TE_{00} , other modes (TE_{10} , TM_{00} , and TM_{10}) have large mode areas and overlap with the rough sidewall and thus undergo a higher scattering loss. As a result, except for the TE_{00} mode, the gain of the other modes was effectively suppressed. In the experiment, the designed single microring realized single-mode lasing at $\sim 1531 \text{ nm}$ with a 35.5-dB SMSR

under the 1484-nm laser source pump with the assistance of the gain competition, as shown in Fig. 7(b). The lasing signal power is up to 2.1 μW , and a threshold of 14.5 mW and a conversion efficiency of 1.20×10^{-4} were inferred by linearly fitting the signal power data. In addition, the wavelength shift with the increasing pump power caused by the photorefractive effect was also observed. The linewidth of the single-frequency laser was measured as 0.9 MHz by a self-heterodyne approach.

Further, Lin et al. realized a single-frequency ultranarrow linewidth laser on a single microdisk, taking advantage of the polygon modes with high-quality factors and sparse mode distribution.⁸⁴ The microdisk with a diameter of $\sim 29.8 \mu\text{m}$ was prepared on a Z-cut 1% erbium-doped LNOI wafer. In experiments, the polygon modes for both pump ($\sim 968 \text{ nm}$) and signal (1550-nm band) were excited by adjusting the coupled tapered fiber to a proper position, as shown in the inset of Fig. 7(c). Because the signal polygon mode has a large FSR (11.5 nm) and overlaps with the pump polygon mode, the gain of the conventional high-density WGMs was effectively suppressed. Accordingly, the single-frequency lasing with a threshold of $\sim 25 \mu\text{W}$ and a maximum SMSR of 37 dB was achieved in the gain band of erbium ions, as shown in Fig. 7(c). The output power of up to 2 μW was obtained at a pump power of 20 mW. The microlaser linewidth was assessed as low as 322 Hz by heterodyning two separately pumped single-mode microlasers. Moreover, a microelectrode with a radius of 5 μm was fabricated on the microdisk to investigate the wavelength tuning using the strong electro-optic effect of LN. As shown in Fig. 7(d), a linear tuning efficiency of 0.5 pm/V was achieved when the applied voltage was tuned from -300 to 300 V. The demonstrated ultranarrow linewidth microlaser would facilitate highly coherent applications based on an LNOI integrated platform.

In addition, Liang et al. also demonstrated a single-frequency microlaser based on an erbium-doped LNOI microring with the shape of quarter Bezier curves.⁸⁵ The signal spectra in the wavelength range of 1500 to 1600 nm with a single-frequency lasing were recorded with the increasing pump power of a 976-nm laser, as shown in Fig. 7(e). The reason for realizing single-frequency lasing was probably mode-dependent loss and gain competition by comparing the transmission spectrum of the microring and the amplified spontaneous emission (ASE) spectrum in the waveguide. For a similar mechanism, Zhu et al. observed a single-frequency lasing with an SMSR of 29.12 dB based on an electro-optically tunable erbium-doped LNOI microdisk, as shown in Fig. 7(f).⁸⁶ In addition, the wavelength of lasing mode was realized through continuous tuning in a 45 pm range by applying the electric voltage from -200 to 200 V.

With the continuous attention and efforts of researchers, microdisks, microrings, and microdisk-microring coupling lasers have been realized based on the REI-doped LNOI platform, and the working state of the laser has also been improved from multimode to single mode. Table 1 summarizes the main performance parameters of the REI-doped LNOI microlasers reported so far. Based on the current research results, we discuss the main limitations and potential solutions for the development of REI-doped LNOI lasers.

Low output power (μW -level) and conversion efficiency. At present, the conversion efficiency and output power of the reported lasers are still at a relatively low level of microwatts in either multimode or single-mode operation, which hinders

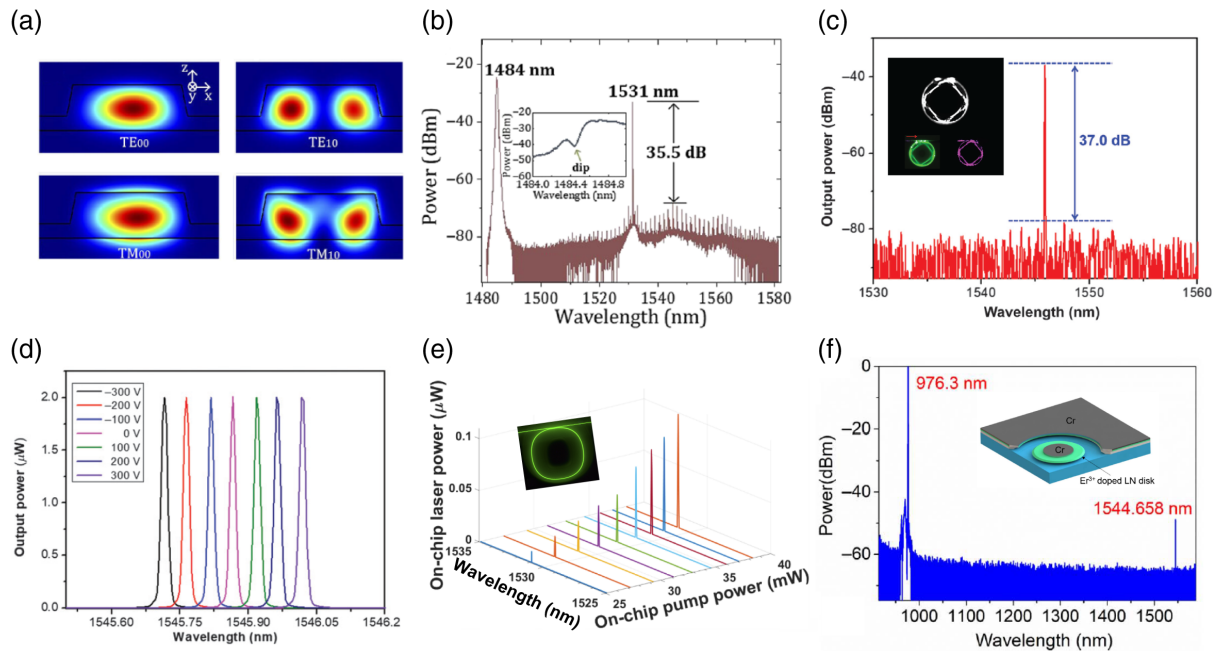


Fig. 7 (a) Simulated mode profile for the four supported modes. (b) Collected single-mode laser emission spectra. Inset: the pump spectra after passing through the microring. (a) and (b) Reprinted from Ref. 83 under a CC-BY license. (c) Observed single-mode laser with a 37 dB SMSR. Inset: a captured image of the excited polygon modes for lasing signal, upconversion fluorescence, and pump, respectively. (d) Single-mode lasing wavelength at different applied voltages. (c) and (d) Reprinted from Ref. 84 under a CC-BY license. (e) Recorded signal spectra in the range of 1500–1600 nm with increasing pump power. Inset: the observed green upconversion fluorescence of the pumped microring. Reprinted from Ref. 85, © 2022 Optica. (f) Observed single-frequency lasing spectrum at 1544.658 nm with a pump power of 18 mW. Inset: the electrode configuration schematic of the tunable microdisk laser. Reprinted from Ref. 86.

the further integration of the laser with other functional devices. We believe that there are several ideas to improve the output power of lasers. (i) Increase the scale of the resonator. The reported works are based on WGM microcavities with a micrometer-scale radius, which limits the optical gain of the laser within such a small gain volume. Therefore, expanding the scale of the gain resonator is a promising method to improve the laser output power. For example, a high laser output power based on large-sized microdisk cavities⁸⁷ and long waveguides with Sagnac loop reflectors⁸⁸ has been reported recently. Compared with previous work of REI-doped LNOI microlasers, the output power has been improved by an order of magnitude. It should be noted that increasing the cavity length will naturally bring about the impact of multimode resonance, which poses a challenge to the single-mode operation of the laser. The mode screening mechanism for realizing single-mode operation described above needs to be considered in laser design. At the same time, the optimization of coupling between the bus waveguide (or tapered fiber) and resonant cavity for both pump and signal bands, such as introducing the bending waveguide coupling design⁶⁸ to ensure effective pumping and effective extraction of signal light, can also effectively improve the output power and conversion efficiency of the laser. In addition, the waveguide integrated with the Bragg grating resonance structure can effectively increase the cavity length and ensure single-mode operation. The DBR or DFB laser with high output power has been confirmed on the silicon-based integrated photonics platform,^{89–91} which can

provide a reference for improving the laser performance. (ii) Introduction of cladding pumping scheme. Referring to the development of fiber lasers, the design of the cladding pump can effectively improve the pump efficiency of high-power diodes and ensure the single-mode operation of signal light, which plays a key role in developing the high-power fiber lasers.^{92,93} Similarly, based on the LN REI gain platform, coating the gain device with appropriate cladding layers, such as silicon dioxide and silicon nitride, can also improve the pump power in the gain structure. Unlike the optical fiber structure, the waveguide is not a circular symmetric structure and may need a reasonable design to ensure the adequate overlap of the pump light and the gain ions. (iii) Co-doped ytterbium ions. For erbium-doped fiber lasers working in the communication band, co-doped ytterbium ions are often used to increase the output power of the laser.^{94,95} This is because ytterbium ions, as a sensitizer, can effectively transfer energy to erbium ions, improving the luminous efficiency of erbium ions. At the same time, for the LN thin-film platform, erbium and ytterbium ions can be conveniently co-doped in the incorporation process of REIs, so it is expected to improve the output power and conversion efficiency of erbium-doped LN thin-film laser.

Optical pumping scheme. Due to the selection of REIs as the gain medium, the working mechanism of optical pumping for the lasers is necessary, which imposes limitations on using lasers for out-of-laboratory applications, such as gas detection

Table 1 Typical parameters comparison of reported REI-doped LNOI lasers^a.

Devices	Pump		Signal					References
	Wavelength (nm)	Threshold (μ W)	Wavelength (nm)	Power (nW)	Linewidth	Conversion efficiency	Modes or SMSR (dB)	
Disk	974	2.99×10^3	1531.6	~ 40	0.12 nm	4.12×10^{-6}	Multiple	27
	1460	9.31×10^3	1531.6	~ 500	0.14 nm	3.15×10^{-5}	Multiple	
Disk	976	<400	1563.3	~ 140	0.024 nm	1.92×10^{-4}	Multiple	70
Disk	974	292	1531.8	~ 0.4	~ 0.01 nm	6.5×10^{-7}	Multiple	71
Disk	984	103	~ 1060	$\sim 2.5 \times 10^3$	—	5.3×10^{-3}	Multiple	72
Disk	~ 976	21.19	~ 1060	3.7×10^2	~ 0.01 nm	1.36×10^{-2}	Multiple	73
Ring	974	~ 20	1532.4	~ 0.1	~ 0.01 nm	6.61×10^{-7}	Multiple	77
Ring	~ 980	$\sim 3.5 \times 10^3$	~ 1530	~ 35	—	4.38×10^{-5}	Multiple	78
Ring	974	59.32	~ 1060	6.44×10^3	~ 0.01 nm	5.45×10^{-4}	Multiple	79
Coupled disk	977.7	~ 200	1550.5	~ 50	348 kHz	7.0×10^{-5}	Single	80
Coupled ring	979.6	~ 200	1531.1	~ 40	~ 0.005 nm	—	26.3	28
Coupled ring	1484	13.54×10^3	1531	3.1×10^2	1.2 MHz	1.45×10^{-4}	31	82
Ring	1484	14.5	1531.3	2.1×10^3	1.27 MHz	1.2×10^{-4}	35.5	83
Disk	968	~ 25	1546	2×10^3	322 Hz	1.0×10^{-4}	37	84
Coupled disk and ring	974	1.31×10^3	1560.4	~ 95	—	4.41×10^{-5}	31.4	81
Ring	976	24.5×10^3	1530.9	$\sim 1 \times 10^2$	0.045 nm	8.33×10^{-6}	~ 18.8	85
Disk	976	—	1544.7	~ 10	—	—	29.12	86
Disk	980	485.5	1551.68	62.1×10^3	0.11 MHz	4.78×10^{-3}	—	87
Sagnac reflector	980	$\sim 6 \times 10^3$	1544	44.7×10^3	28 pm	1.8×10^{-3}	25	88

^aAll results are approximate values obtained from the reported literature.

and biosensing. A practical solution is to integrate a commercial semiconductor laser as the pump source for the LNOI laser. For example, the electrically pumped laser and REI-doped chip can be hybrid integrated by the flip-chip technology, which is expected to effectively improve the portability of the laser. Zhou et al. reported the pioneering work demonstrating the electrically pumped REI-doped LNOI laser for the first time by butt-coupling a laser diode chip with an erbium-doped LN gain chip.⁹⁶ In addition, the electrically pumped REI-doped LN lasers can also be realized by heterogeneously integrating III-V materials on REI-doped LN chips to construct the pump laser.⁹⁷ It should be mentioned that compared with the electric pump laser realized by direct hybrid integration or heterogeneous integration, REIs have a long excited-state lifetime, resulting in REI-doped LNOI lasers with low signal noise and narrow linewidth, which has advantages for developing applications, such as optical coherent communication and quantum optics.

Wafer global doping. As mentioned in the previous introduction, the LN thin film cannot tolerate the high temperature conditions required by thermal diffusion or ion implantation to achieve high-concentration doping. Therefore, the method of incorporating REIs into LN thin film for the currently reported REI-doped microlasers is mainly doping in the growth process of bulk LN before ion slicing. However, one of the side effects of this doping method is that REIs are distributed on the entire LN thin-film wafer, which brings additional absorption loss and refractive index changes to the passive device integrated on the same chip, degrading the device's performance. There are

several ways to realize local doping. (i) Before the LN thin film is formed by ion slicing, bulk LN wafers can be doped locally with REIs by thermal diffusion or ion implantation. Rüter et al. prepared a neodymium-doped LN thin film by thermal diffusion doping before ion slicing, which confirmed the possibility of local doping by this method.⁵⁷ At the same time, it should be noted that incorporating REIs by thermal diffusion or ion implantation may pose a challenge to the sliced thin film quality. For example, Xu et al. reported that the thermal diffusion doping process increases the roughness and causes a slight deformation at the diffusion surface of the erbium-doped LN wafer.⁶¹ An additional CMP step before the ion slicing process is expected to improve this diffusion surface quality. (ii) Integrated REI-doped LN thin film with undoped LN thin film by butt-coupling to construct active-passive LN thin-film devices. For example, Zhou et al. reported the work of tiling erbium-doped LN film and undoped LN film with ultraviolet curing adhesive and then prepared the monolithically integrated amplifier using a single continuous photolithography process based on the active-passive chip.⁹⁸ The limitation of this method is that due to the integration of two different chips, the thickness may vary, resulting in an additional loss at the optical interface of active and passive chips. At the same time, the scalability and stability of large-scale integration for this method have certain limitations due to splicing the two independent chips. (iii) Hybrid REI material on LN thin film. Another promising scheme for localized incorporation of REIs is to deposit materials locally with REI gain media on LN thin film. For example, REI-doped TeO₂ and REI-doped Al₂O₃ materials were widely used in

active integrated photonics for their high rare-earth solubility, large emission cross section, as well as wafer-level deposition techniques.^{99,100} One consideration in this design is that sufficient overlap between the pattern of the LN layer and the gain material is required to obtain large gains or power output, for example, by depositing the gain material into the microtrenches design to improve the gain performance of the device.^{101,102} In addition, by introducing the design of REI-doped loaded waveguide, the fabrication process of active devices based on LNOI can be simplified. For example, silicon nitride materials featuring low transmission loss, refractive index close to LN, and CMOS compatibility are successfully applied on the LNOI platform.^{103,104} Some other aspects still need to be explored. The locking of the pump mode and the encapsulation of the coupling region deserve to be explored in the experiment to obtain high output power and stable operation of the laser during high-power pumping. Moreover, the wavelength tunability of the reported single-mode lasers is also limited. The thermo-optic effect of LN crystal can be utilized to achieve broadband wavelength tuning by integrating microheaters on the coupled resonators.¹⁰⁵ Furthermore, combined with the outstanding electro-optical properties of LN, the REI-doped LNOI laser provides a promising platform for fundamental physics research, such as PT-symmetry breaking with natural advantages.^{106,107}

2.3 Amplifiers Based on REI-Doped LNOI

In addition to lasers, amplifiers can provide gain for on-chip signals and therefore have fairly broad-based demand in on-chip optical communication, nonlinear frequency conversion, and other applications. High-gain waveguide amplifiers based on silicon nitride and integrated silicon platforms have been proven to be successful.^{108,109} However, due to the weak optical confinement as well as nonuniform distribution of REIs in titanium-diffused channel waveguide, the gain performance of waveguide amplifiers based on bulk LN is generally low (<3 dB/cm).¹¹⁰ Fortunately, as mentioned above, waveguides prepared based on REI-doped LNOI can obtain strong mode localization and high doping concentration with uniform distribution, which lays the foundation for the realization of large-scale integrated high-gain LNOI waveguide amplifiers. Consequently, the research on REIs-doped LNOI amplifiers has also attracted the attention of researchers.

Zhou et al. demonstrated the first waveguide amplifier on a Z-cut 600 nm-thick erbium-doped LNOI chip with 1% doping concentration.¹¹¹ The 3.6-cm-long waveguide amplifier with a spiral design to reduce the overall device size was fabricated by the PLACE process. The signal gain at 1530 nm under different pump power was measured with a fixed on-chip signal power of 19.64 nW by a bi-directional pumping scheme. Then, considering the propagation loss calibration, the internal net gain for this signal wavelength was obtained by the equation

$$g = 10 \log_{10} \frac{P_{\text{on}}}{P_{\text{off}}} - \alpha L, \quad (3)$$

where P_{on} and P_{off} are the measured signal powers in pump-on and pump-off state and α and L denote the transmission loss coefficient at the signal wavelength and the corresponding waveguide length, respectively. As shown in Fig. 8(a), the internal net gain exhibits a rapid rising stage (small-signal gain)

and a gradual trend to gain saturation process following the growing pump power. A maximum internal net gain of 18 dB was achieved at the pump power of ~40 mW. At the same time, the strong green upconversion fluorescence in the waveguide was observed when the amplifier is operating, as shown in the inset of Fig. 8(a), which was investigated by Jia et al., who found a dual-color upconversion luminescence emission.¹¹⁶ The signal gain at different wavelengths was measured and consistent with the signal fluorescence spectrum, as shown in Fig. 8(b). In addition, the polarization dependence of amplifier gain was studied under different polarization states for both pump and signal modes. As a result, the maximum gain was obtained where pump and signal modes all have a TE polarization. This probably is due to that the TE modes in Z-cut erbium-doped waveguide have better absorption and emission cross sections for the pump at the 980-nm band and signal at the 1550-nm band, respectively. At the same time, the low transmission loss for TE polarization also contributes to obtaining a high gain. Additionally, the same group recently demonstrated a four-channel erbium-doped waveguide amplifier with a net gain of ~8 dB at 1530 nm based on a monolithically integrated active-passive LNOI chip.⁹⁸

At the same time, Chen et al. fabricated a compact 5-mm-long waveguide amplifier using the EBL-Ar⁺ etching and CMP process based on an erbium-doped LNOI with 0.5% doping concentration.¹¹² Under the 980-nm laser source pump, the measured signal spectra for the increasing pump power in the range of 0 to 21 mW are shown in Fig. 8(c). The maximum internal gain at 1531.6 nm is about 5.2 dB, corresponding to a net gain per unit length of >10 dB/cm. The internal conversion efficiency was deduced up to 0.2% with the equation $\eta = 100\% \times (P_{\text{on}} - P_{\text{off}})/P_{\text{pump}}$, where P_{pump} is the pump power. In addition, they also demonstrated a 4.3-mm-long erbium-doped LNOI waveguide amplifier with a signal enhancement factor of 5.4 dB cm⁻¹ at a low pump power of 3 mW.⁶¹

Subsequently, Luo et al. reported on-chip erbium-doped LNOI waveguide amplifiers based on a similar simplified fabrication process without Cr film deposition and CMP steps.¹¹³ The amplifiers consist of a compact straight waveguide with a length of 5 mm. The doping concentration of erbium ions is 0.1%, which is much lower than that in previous reports. Under the 974.3-nm laser pump, the net internal gain at 1531.5 nm with a fixed signal power of 5 nW was investigated by increasing the pump power. A maximum net internal gain of 5.5 dB was obtained at a higher pump power of ~64 mW. In addition, the gain dependence on the signal power at 1531.5 nm with a fixed pump power (23 mW) was measured and is shown in Fig. 8(d). What is more, a maximum internal net gain of 15 dB at -65 dBm signal power is achieved. The internal net gain per unit length is up to 30 dB/cm, which is the highest value for the reported REI-doped LNOI waveguide amplifiers. It should be mentioned that the optimal gain is obtained under a weak signal power (-65 dBm), so the amplifier may be more suitable for small signal amplification, sensing, and other related fields.

To enhance the integration density of devices, Yan et al. also fabricated a 1% erbium-doped LNOI waveguide amplifier with a spiral design using the EBL-Ar⁺ etching process.²⁹ The waveguide has a total length of 5.3 mm with a footprint of ~0.06 mm². To characterize the spiral waveguide amplifier net gain, two lasers operating at 974 nm were used for the bi-directional pump. A maximum net gain of 8.3 dB at 1530 nm

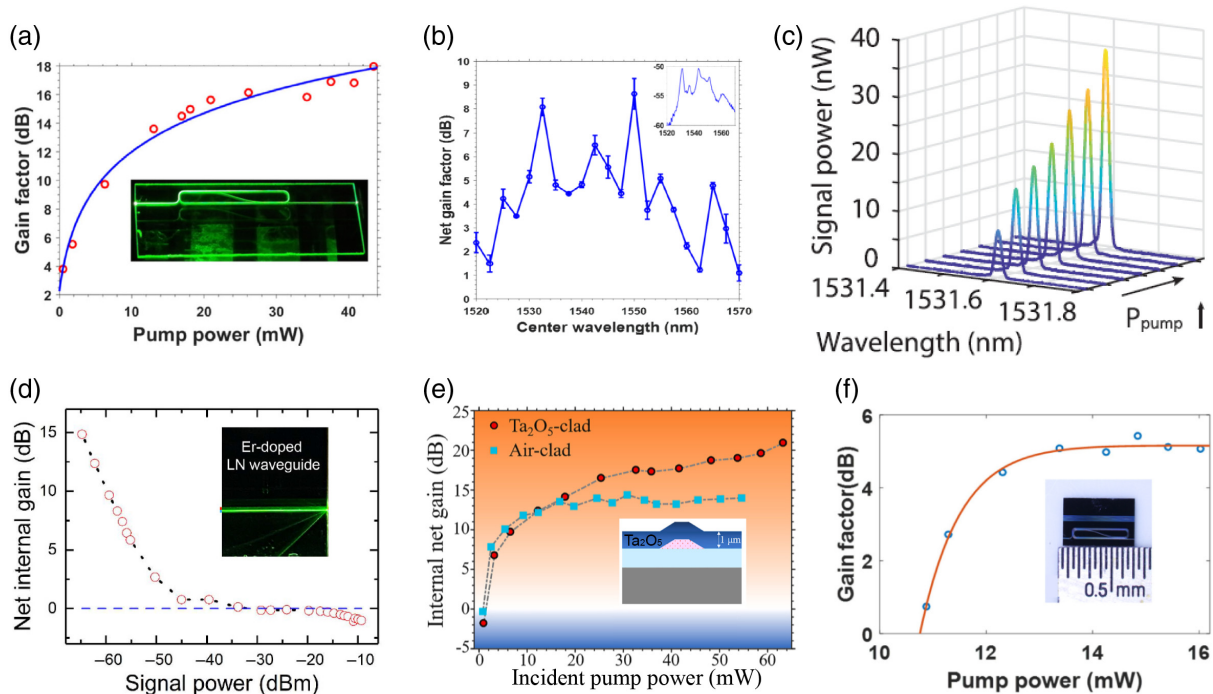


Fig. 8 (a) The obtained internal net gain at 1530 nm with increasing pump. Inset: observed green upconversion fluorescence under the 980 nm laser pump. (b) The measured signal gain at different wavelengths. Inset: spontaneous spectrum measured in erbium-doped LN waveguide. Inset: detected spontaneous spectrum measured in erbium-doped LN waveguide. (a) and (b) Reprinted from Ref. 111. (c) Measured signal spectra as a function of increasing pump powers measured at 1531.6 nm. Reprinted from Ref. 112, © 2021 Optica. (d) Dependence of internal net gain at 1531.5 nm on the signal power. Inset: observed green upconversion fluorescence in the compact waveguide. Reprinted from Ref. 113. (e) The measured net gain for Ta₂O₅-clad waveguide amplifiers and Air-clad waveguide amplifiers. Inset: the cross-sectional schematic of the erbium-doped LNOI waveguide amplifiers with Ta₂O₅-cladding. Reprinted from Ref. 114 under a CC-BY license. (f) The measured net gain of ytterbium-doped LNOI waveguide amplifiers at the different pump powers and the signal wavelength of 1060 nm. Inset: the photograph of the ytterbium-doped LNOI waveguide. Reprinted from Ref. 115 under a CC-BY license.

was obtained, which is considered equivalent to a net gain per unit length of ~ 15.6 dB/cm. At the same time, the net internal gain in the 1520 to 1570 nm range was characterized and showed that the majority wavelength range could obtain an over 3 dB net gain.

In addition, inspired by the design of double-cladding fiber, Liang et al. fabricated ~ 10 -cm-long tantalum pentoxide (Ta₂O₅)-clad erbium-doped LNOI waveguide amplifiers by depositing a ~ 1 - μ m-thick layer of Ta₂O₅ on the top of LN waveguide core, as shown in the inset of Fig. 8(e).¹¹⁴ As part of the optical power in the LN core is introduced into the cladding waveguide, the detrimental absorption of pump power and signal powers by quenching ions is reduced. The optical gain of the waveguide amplifiers with Ta₂O₅-cladding was measured and shown to be superior to the amplifiers without cladding, with a maximum net gain of more than 20 dB at 1532 nm, as shown in Fig. 8(e). Recently, ytterbium-doped LNOI waveguide amplifiers fabricated by the PLACE process were reported by the same group.¹¹⁵ The maximum net gain at 1060 nm for a 4-cm-long waveguide [the inset of Fig. 8(f)] pumped by a 976-nm laser was measured at about 5 dB, as shown in Fig. 8(f).

Also, the influencing factors, such as pump wavelength, pump mode, and waveguide length for the performance of the amplifier were carefully investigated by Cai et al. based on an erbium-doped LNOI waveguide amplifier with a concentration of 0.72×10^{20} cm⁻³.¹¹⁷ An internal net gain of 16 dB at 1531.6 nm with a saturation power of -8.84 dBm was achieved on a 2.5-cm-long waveguide, as shown in Fig. 9(a). The amplifier noise figure mainly originates from spontaneous emission and shows a trend of increasing with the signal power. Experimentally, the minimal noise figure of 4.49 dB at -50 dBm signal power and near 6 dB in the range of signal power from -45 to -28 dBm was observed, as shown in Fig. 9(b). In addition, the power conversion efficiency reflecting the pump effectiveness was characterized and displayed a trend of decreasing with the increasing signal power due to the reduction of the obtained internal gain, as shown in Fig. 9(c). Moreover, although the absorption coefficient of erbium ions in the 980-nm band is higher than 1480-nm band,¹¹⁸ the amplifier operating on the 1484-nm pump exhibits a higher gain than on the 980-nm pump, as shown in Fig. 9(d), which is mainly because the 1484-nm pump has a better overlap factor with signal and a lower transmission loss. The gain performance

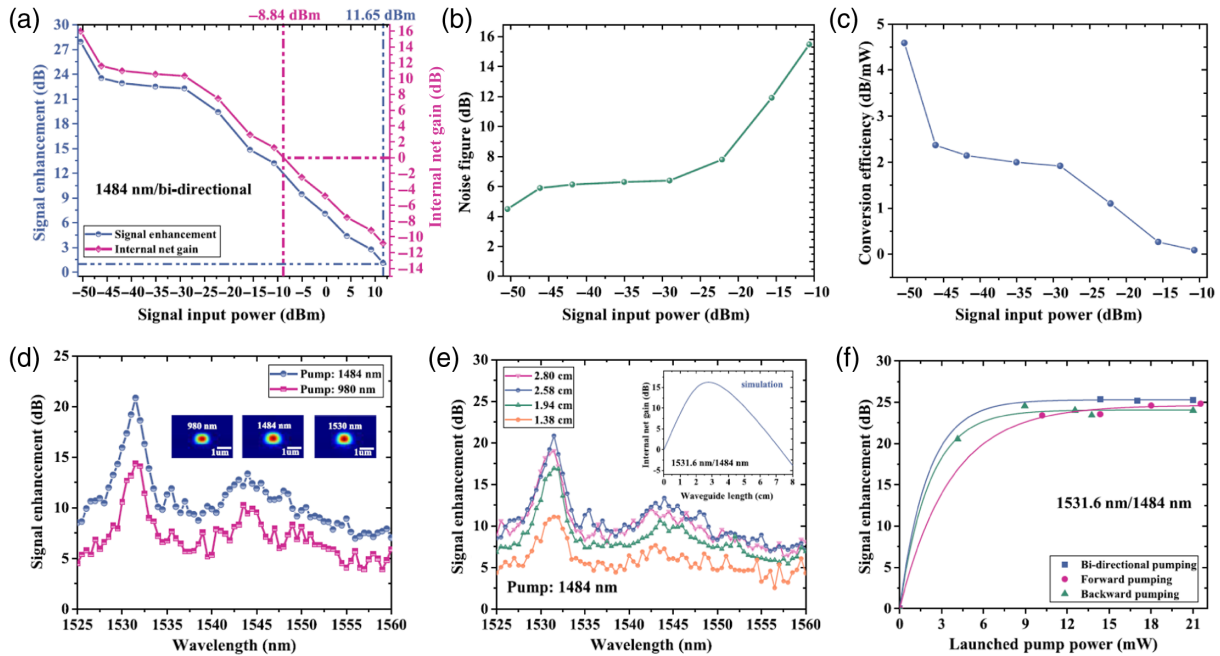


Fig. 9 (a) The measured signal enhancement and internal net gain at different signal input power at 1531.6 nm. (b) The noise figure and (c) the pump power conversion efficiency for different signal input power at 1531.6 nm. (d) The comparison of signal enhancement between 980 nm and 1484 nm pumps. Inset: modes distribution at 980 nm, 1484 nm, and 1530 nm. (e) The comparison of signal enhancement for different waveguide lengths. Inset: the simulation internal net gain at 1531.6 nm as a function of waveguide lengths. (f) The signal enhancement for different pumping schemes at 1531.6 nm. (a)–(f) Reprinted with permission from Ref. 117, © 2022 IEEE.

for different waveguide lengths was also studied, as shown in Fig. 9(e). The optimal length of 2.58 cm close to the simulation value of 2.68 cm was observed. Additionally, the pumping scheme was also studied in this work. Specifically, for forward pumping, the pump power is high at the front end and low at the back end, while the signal is opposite. Thus, for an amplifier with a long waveguide length or high doping concentration, when the signal light is transmitted to the back end, the remaining pump power is insufficient to provide sufficient gain, resulting in overall gain performance degradation. Although backward pumping can be applied to avoid the power distribution mismatch and obtain a greater gain, this pumping scheme will introduce a higher noise. Therefore, bi-directional pumping is often used to balance gain and noise performance. As shown in Fig. 9(f), a better gain and noise performance was obtained at the bi-directional pumping scheme compared to forward pumping and backward pumping.

As can be seen from the above introduction, amplifiers with straight and spiral oxide cladding waveguide structures have been successfully verified based on REI-doped LNOI platforms. The pumping wavelength and pumping scheme of amplifiers are also explored. Table 2 summarizes the key parameters of REI-doped LNOI waveguide amplifiers reported so far. However, there are still several problems that need to be resolved in the development of amplifiers, as discussed below.

2.3.1 High output power

Although a maximum net gain factor of 20 dB was realized based on a 10-cm-long waveguide. The high gain of the amplifier is obtained at the low input signal power (−22 dBm), which

leads to the low output power of the amplifier and limits the application scenarios of the amplifier to a certain extent. To further improve the gain performance of the amplifier, especially for high signal power amplification, the most important problem to be solved is to reduce the propagation loss of the waveguide, which limits the available REI-doped waveguide length and, therefore, the attainable output power level.¹²⁰ For example, a promising reference work is that Liu et al. achieved a signal output power of 145 mW with a signal input power of 2.61 mW based on a 0.21-m-long erbium-doped silicon nitride waveguide with a doping concentration of $\sim 3.25 \times 10^{20} \text{ cm}^{-3}$.¹²¹ The propagation loss based on this silicon nitride platform is $< 5 \text{ dB/m}$, which is far lower than the reported value of LNOI erbium-doped amplifiers (an optimal value of 16 dB/m).¹¹¹ Therefore, it is expected to obtain higher output power on a longer REI-doped waveguide by improving the processing technology. Moreover, the REI doping concentration and the mode overlap factor between the optical mode and REIs can be further optimized for more significant gain. In addition, for the amplification of high signal power, the coupling of the on-chip waveguide and off-chip pump is also a special concern. Due to the long REI-doped waveguide and high input signal power, higher requirements for on-chip pump power are also put forward. Therefore, it is necessary to introduce a high-efficiency coupler in the pump band or adopt a multichannel pumping scheme to meet the pump power requirement of the amplifier and avoid degradation of amplifier performance. In addition, a high erbium ion doping concentration is usually required for the short waveguide amplifier to obtain high gain. However, the high doping concentration will cause some detrimental effects, such

Table 2 Typical parameters comparison of reported REI-doped LNOI amplifiers^a.

Waveguide		Pump			Signal					Ref.
Length (cm)	Doping concentration (%)	Wavelength (nm)	Power (mW)	Pumping schemes ^b	Wavelength (nm)	Power (dBm)	Internal net gain (dB)	Gain per unit length (dB/cm)	Output power (dBm)	
3.6	1	980	40	Bi	1530	-47.	18	5	-29.07	111
			26	Bi	1550	-38.38	7.5	2.08	-30.88	
0.5	0.5	980	21	For	1531.6	-50.86	5.2	10.4	-45.66	112
			21	For	1550	-52.37	1.8	3.6	-50.57	
0.5	0.1	974	~23	For	1531.5	-65	15	30	-50	113
0.53	1	980	10.78	Bi	1530	-10.7	8.3	15.66	-2.4	29
2.8	1	980	45	For	1531.6	—	8.45	3.02	—	119
2.58	1	1484	17.31	Bi	1531.6	-50	16	6.20	-34	117
		1484	18.54	Bi	1550	-50	2.66	1.03	-47.34	
10	1	976	63	Bi	1532	-22	20	2	-2	114
4	0.5	976	16	For	1030	—	5	1.25	—	115
		976	48	For	1060	—	8	2	—	
2	—	976	14	For	1530	—	8	4	—	98
					1550	—	5	2.5	—	

^aAll results are approximate values obtained from the reported literature.

^bFor, forward pump; Bi, bi-directional pump.

as cooperative upconversion and concentration quenching, thus degrading the amplifier gain performance. The introduction of ytterbium ions with a similar absorption band near 980 nm is expected to achieve high amplifier gain over shorter waveguide lengths by reducing the detrimental effects through energy transfer,^{110,122} which can be explored in the research of the erbium-doped LNOI amplifier.³⁶

2.3.2 L-band amplification

At present, the erbium-doped LNOI waveguide amplifiers confirmed work in the C-band (1530 to 1565 nm), and there is no research report on L-band (1565 to 1625 nm) LNOI amplifiers. However, it is very important to expand the bandwidth of on-chip communication. Because the emission cross section of erbium ion in LN at the L-band is much lower than the C-band, it is necessary to accumulate the gain with a longer waveguide length than the C-band amplifier to achieve the L-band amplification. Referring to the research of L-band erbium-doped fiber amplifier (EDFA),¹²³ there are some methods to improve the L-band gain of the erbium-doped LNOI waveguide amplifier. (i) Since the signal to be amplified is in the L-band, the ASE in the C-band can also be used for pumping to improve the gain. For example, a C-band high-reflectivity grating structure can be introduced at the input end of the erbium-doped waveguide to recycle the unused backward ASE. (ii) An auxiliary pump light working at 1550 to 1560 nm can be introduced to enhance the L-band gain.

2.3.3 Gain flattening amplification

Another problem that needs attention is the gain flatness of the erbium-doped LNOI amplifier, which is particularly important in optical communications based on on-chip wavelength

division multiplexing. Because the gain of an erbium ion is not flat in the broadband range, many studies have been done based on the erbium-doped fiber amplifier system to obtain the flat gain. The basic idea is to introduce a filter so that the changing trend of transmission loss relative to wavelength is consistent with that of the gain relative to wavelength and thus obtain broadband and flat gain. For example, Mach-Zehnder filter,¹²⁴ acousto-optic filter,¹²⁵ and long-period fiber grating¹²⁶ have been used in EDFA to achieve wide flat-band gain. In addition, a dual-core fiber design was demonstrated to obtain an ultra-wide-band gain-flattened EDFA by regulating the coupling between parallel transmission fibers.¹²⁷ With the excellent photoelectric and acousto-optic properties of LN and the mature micro-nano processing technology of LNOI, the design experience based on the EDFA system can be conveniently transferred to the LNOI platform and hopefully achieve better gain flatness.

2.3.4 Some other limitations

The reported amplifiers mainly operate in the communication band. There is less research on amplifiers in other bands, which can be effectively expanded by doping with different REIs, such as neodymium and thulium.¹²⁸ In addition, the problems of optical pumping and local doping of REIs also exist, which can be referred to in the previous discussion on REI-doped microlasers.

3 Electrically Pumped III-V Lasers and Amplifiers on LNOI Platform

In addition to REI doping, introducing III-V material as a gain medium is another common method to realize an integrated light source and amplifier. Because the laser and amplifier based on III-V material can work through direct electric pumping, it has

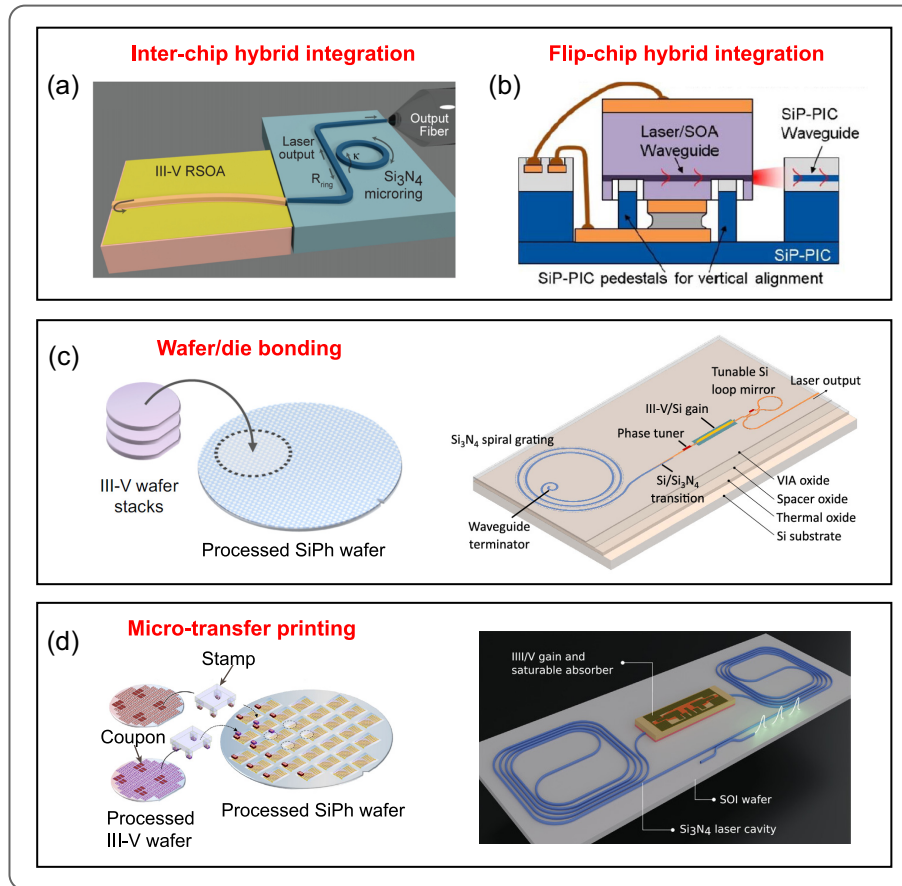


Fig. 10 The integrated schemes for electrically-pumped integrated photonics gain devices. (a) Schematic diagram of a typical inter-chip hybrid integrated laser. Reprinted from Ref. 135, © 2017 Optica. (b) Schematic diagram of a flip-chip hybrid integrated laser. Reprinted from Ref. 136, © 2017 Optica. (c) Left, illustration of heterogenous integration for wafer bonding. Reprinted from Ref. 134 under a CC-BY license. Right, schematic diagram of a heterogenous integration narrow-linewidth III-V/Si/Si₃N₄ laser realized by the wafer bonding techniques. Reprinted from Ref. 137, © 2022 Optica. (d) Left, illustration of micro-transfer printing technology. Reprinted from Ref. 129 under a CC-BY license. Right, schematic diagram of a heterogenous III-V-on-silicon-nitride mode-locked comb laser realized by the micro-transfer printing techniques. Reprinted from Ref. 138 under a CC-BY-NC-ND license.

the advantages of high gain efficiency and portability. It thus has become the mainstream route to develop integrated photonics gain devices. At present, the way to integrate an electric pump light source based on III-V gain materials with an LNOI platform can be roughly divided into hybrid integration, heterogeneous integration, and microtransfer printing, as described below.^{129–134}

Hybrid integration is one of the most mature integration technologies that assembles several fully processed chips, such as III-V semiconductor devices and passive integrated photonics devices, into a single multifunctional device at the last packaging stage. Moreover, it can test and optimize discrete devices before integration to ensure the yield of integrated device products. Based on the current commercial mature small size III-V gain chip with high power and efficiency (such as support from Freedom Photonics LLC), namely, electrically pumped laser or semiconductor optical amplifier chip, there are mainly inter-chip hybrid integration and flip-chip hybrid integration methods

used to realize an integrated active device. (i) Inter-chip hybrid integration. The active chip is assembled adjacent to the passive integrated external cavity chip and introduces gain through butt coupling. For example, Fig. 10(a) shows that the off-chip reflective semiconductor optical amplifier and the low-loss silicon nitride micro-ring external cavity chip are placed next to each other to realize the electrically pumped compact narrow linewidth integrated laser.¹³⁵ To improve the optical coupling efficiency of the gain chip and the external cavity chip, the optical waveguides of the two chips should be aligned. A spot-size converter design is usually introduced in the optical interface of the passive chip. (ii) Flip-chip hybrid integration. The active chip is assembled on a solder bumps recess at the passive chip by the pick-and-place method. A schematic diagram of a hybrid silicon photonic flip-chip laser is shown in Fig. 10(b), and vertical alignment accuracy of ± 10 nm is achieved by adjusting the etching thickness of pedestals.¹³⁶ Compared with inter-chip integration, the flip-chip process has a higher integration degree,

and the stability and thermal management of devices have also been improved. However, during the assembly process, both hybrid integration methods require high alignment accuracy, especially the flip-chip process demanding both horizontal and vertical directions, and can only integrate almost a singular chip at a time, which slows down the integration process and raises the cost of integrated chips, making hybrid integration technology a challenge in mass production.

Heterogeneous integration is an integration technology that bonds III-V thin film wafer or dies to the top of a processed base wafer at the intermediate stage, as shown in the left panel of Fig. 10(c).¹³⁴ Then the unprocessed III-V material is fabricated to the III-V gain devices, such as laser or amplifier arrays, by the lithography-etching process with a wafer-level scale. Due to the III-V devices being defined by the lithography process, an ultrahigh alignment accuracy for the light source and the passive device is realized by the adiabatic coupling at the interfaces between different layer waveguide structures to ensure an effective coupling. The right part of Fig. 10(c) shows the schematic diagram of a narrow-linewidth III-V/Si/Si₃N₄ laser based on wafer bonding techniques.¹³⁷ Compared with hybrid integration, heterogeneous integration technology has the advantages of wafer-level productivity and high alignment accuracy defined by lithography, which effectively improves the integration density, alleviates the dependence on high alignment tools, and reduces the cost. However, heterogeneous integration cannot test the prepared III-V or passive devices in the intermediate process, resulting in a lower yield of products, which can be improved by improving the maturity of the process.

Microtransfer printing is another popular technique that can pretest III-V devices before integration and enables a large-scale parallel integration, which elegantly combines the advantage of flip-chip hybrid integration and heterogeneous integration techniques. As shown in the left panel of Fig. 10(d), different from the wafer bonding technique, the laser or amplifier devices are prefabricated on the native III-V wafer before transfer to the processed wafer. In the microtransfer printing process, a polydimethylsiloxane (PDMS) stamp is used to pick up the prefabricated active devices (referred to as coupons) with an underneath release layer and transfer them to the passive devices with a single or arrays form.¹²⁹ The alignment between the coupons and the passive device is realized by the digital pattern recognition based on the markers defined on the III-V wafer and base wafer in the prefabricated process. At present, an alignment accuracy of $\pm 1.5 \mu\text{m}$ (3σ) for transfer arrays and $< 1 \mu\text{m}$ for transfer single coupons is realized by the state-of-the-art microtransfer printing tools, which is still lower than the wafer bonding approach.¹³⁹ The right part of Fig. 10(d) shows a schematic diagram of a low noise III-V-on-silicon-nitride mode-locked comb laser demonstrated by the microtransfer printing techniques.¹³⁸

Compared to wafer bonding techniques, microtransfer printing technology can achieve high-yield integration and does not need to adjust the back-end process flow due to the parallel processing of III-V devices and passive devices and the short transfer cycle. In addition, microtransfer printing techniques can reuse the expensive III-V native substrate, which reduces the cost to a certain extent. On the other hand, the wafer bonding approach has a high alignment accuracy and thus provides great advantages in optical coupling efficiency between active devices and passive devices and scalability. A more comprehensive introduction and discussion of the three basic integration

approaches can be found in recent reviews.^{129,132} Based on the integration schemes of the above primary III-V gain devices, the electrically pumped III-V lasers and amplifiers based on the LNOI platform have also been developed, as presented in this section.

3.1 Hybrid Integration III-V Lasers

Han et al. first integrated an electrically pumped III-V laser with a passive LNOI chip.³⁰ To realize broadband tuning and single-mode lasing, the LNOI chip incorporates a Vernier filter consisting of two cascaded microring resonators and a distributed Bragg reflector with a Gaussian apodization profile, as shown in Fig. 11(a). The hybrid laser has a threshold current of 100 mA corresponding to a threshold current density of 2.5 kA/cm^2 and maximum on-chip power of 2.5 mW. With the assistance of the incorporated Vernier filter, the SMSR of the hybrid single-mode laser achieved up to 60 dB at 1325.5 nm. In addition, the broadband wavelength tuning of the lasing signal was performed by applying voltages on the thermo-optic heater integrated with the microring. As shown in Fig. 11(b), the observed superimposed spectra of coarse tuning with a tuning range of 36.4 nm and a tuning efficiency of 0.42 nm/mW were demonstrated. Furthermore, fine-tuning over a wavelength range of 0.5 nm was achieved by applying voltages on both thermo-optic heaters. Combined with the excellent electro-optical performance of the LNOI platform, this demonstrated hybrid laser shows great potential for the realization of a high-speed optical transmitter by further integrating an LNOI modulator. Subsequently, an O-band LN/III-V transmitter with a wavelength-tuning range of over 40-nm circuit was demonstrated by hybrid integrating an RSOA to an LNOI photonic integrated circuit.¹⁴²

Additionally, Shams-Ansari et al. developed a fully integrated high-power laser on a passive LNOI chip by flip-chip bonding a DFB laser.³³ The LNOI chip was fabricated on an X-cut 600 nm thick LNOI chip by the EBL-Ar⁺ etching process. The buffer layer thickness of SiO₂ was chosen to be $4.7 \mu\text{m}$ for the optical mode match in height between the DFB laser and LNOI waveguide. In addition, to ensure maximum overlap of the optical modes between the DFB laser and chip waveguide, a horn coupler with an out-taper width of $8 \mu\text{m}$ was introduced in the butt coupling region, as shown in Fig. 11(c). The waveguide width is designed to be 800 nm to ensure a single-mode operation. The light-current (L-I) curve of the hybrid laser was measured under an electrical pump applied by a source meter, as shown in Fig. 11(d). Thanks to the high output power of the DFB laser and the optimization design of the coupling between the DFB laser and LNOI chip, the on-chip optical power of the hybrid laser was up to 60 mW at 1.0 A current under room temperature, which is the highest reported value for LNOI integrated photonics platforms. Meanwhile, the single-mode spectrum was observed, and the linewidth was characterized as below 1 MHz using a delayed self-heterodyne technique. Furthermore, to explore applications of the hybrid LNOI laser in telecommunication spaces, a high-power laser transmitter was assembled by integrating an LNOI electro-optic modulator with the DFB laser. The demonstrated hybrid integrated laser transmitter effectively promotes the application of LNOI systems in long-haul telecommunication, data center interconnection, and other related fields.

In addition, Kippenberg's group reported a heterogeneous Si₃N₄-LiNbO₃ integrated platform via direct wafer bonding, as shown in Fig. 11(e).¹⁴⁰ Combining the ultralow-loss merit

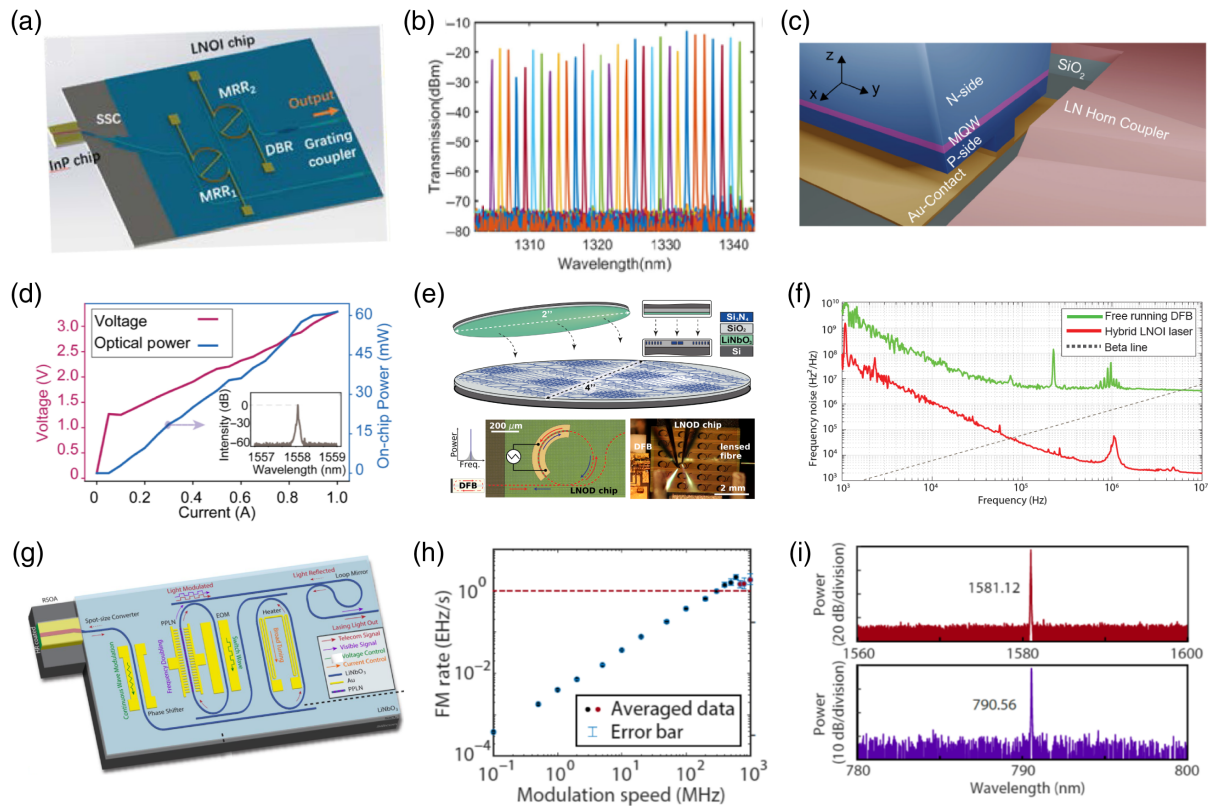


Fig. 11 (a) Schematic of the tunable hybrid LNOI/III-V laser composed of an InP-based optical gain chip and an LNOI passive chip. (b) Recorded spectra of coarse wavelength tuning process. (a) and (b) Reprinted from Ref. 30, © 2021 Optica. (c) Schematic of the butt coupling of the electrically pumped hybrid laser. (d) Optical power inside the LNOI waveguide laser and voltage versus the laser driving current. Inset, the recorded lasing spectrum with the single-mode operation. (c) and (d) Reprinted from Ref. 33, © 2021 Optica. (e) Schematic illustration of lithium niobate integrated on Damascene platform (top) and self-injection locking principle (bottom) with laser wavelength tuning achieved by applying a voltage signal. Reprinted from Ref. 140 under a CC-BY license. (f) Single-sided power spectral density of frequency noise of the hybrid LNOI laser upon self-injection locking to racetrack resonator (red) and in free-running regime (green). Reprinted from Ref. 141. (g) The structure schematic of the hybrid integrated III-V/LNOI external cavity laser. (h) Laser frequency modulation rate as a function of modulation speed. (i) Observed dual-wavelength lasing spectra. (g)–(i) Reprinted from Ref. 34 under a CC-BY license.

of silicon nitride photonic platform and the large Pockels coefficient of LN, the integrated platform realized an ultrafast tunable laser featuring an intrinsic linewidth of 3 kHz and frequency-tuning rate of 12 PHz/s by butt-coupling an InP-based DFB diode laser. Moreover, a proof-of-concept frequency-modulated continuous-wave (FMCW) lidar ranging experiment was performed based on this hybrid integrated laser with a resolution of 15 cm. More recently, this group also demonstrated a frequency-agile LNOI laser by hybrid integrating a DFB laser to LNOI photonic integrated circuits.¹⁴¹ The maximum measured power in the output fiber of the hybrid laser is 1 mW with an SMSR of 60 dB lasing at 1556.3 nm. Compared to the free-running DFB laser, the frequency noise of the hybrid laser is suppressed by more than 20 dB by exploiting the laser self-injected locking effect, as shown in Fig. 11(f). Moreover, the ability of ultrafast frequency actuation of the laser was explored using the Pockels effect of the LN with a 7×10^{11} Hz/s tuning rate and CMOS-compatible driving voltage in the self-injection locked state.

Recently, Li et al. demonstrated an electrically pumped Pockels laser through a hybrid integrated III-V RSOA with an LNOI external cavity structure.³⁴ As shown in Fig. 11(g), the LNOI chip was designed as a Vernier mirror structure consisting of two racetrack resonators. To enrich the functionality of laser and expand its application scenarios, a microheater, electro-optic modulator, phase shifter, as well as a PPLN wavelength converter were incorporated into the LNOI external cavity chip. At the same time, the racetracks and bus waveguides were designed to support only quasi-TE mode to use the significant Pockels effect of LN. The lasing mode at 1581.12 nm with a threshold current of 80 mA was observed in experiments. The on-chip power was measured as ~ 3.7 mW at 200 mA and can be further improved to 5.5 mW by adjusting the Vernier mirror conditions. The laser operated at a single-mode state with a linewidth of 11.3 kHz and an SMSR greater than 50 dB. In addition, the coarse wavelength tuning with a tuning range of 20 nm was realized by thermo-optical tuning of a Vernier ring through the incorporated microheater. To

explore the ultrafast frequency tuning capability, a high-speed driving electrical signal with a triangular waveform was applied to the phase shifter. The laser frequency tuning efficiency and rate under different modulation frequencies were investigated. The tuning efficiency remained at a constant level of (0.26 to 0.34) GHz/V in the broad range of modulation frequency; the frequency tuning rate displayed a linearly increased tendency with the modulation speed, and a value of 2×10^{18} Hz/s was realized at the modulation frequency of 600 MHz, as shown in Fig. 11(h). In addition to the pure frequency modulation, the fast on-off switching of the lasing mode and the switch between two lasing modes with one Vernier FSR were also realized by applying a square wave signal on the driving electrodes of the racetrack resonator. Moreover, the two-color laser was realized by the inherent SHG of the fundamental telecom laser based on the incorporated PPLN frequency-doubling structure, as shown in Fig. 11(i). Benefiting from the large Pockels effect of LN, this demonstrated laser has the essential capabilities of fast tuning and reconfigurability, which holds great potential for application in atomic physics, lidar, and microwave photonics. More recently, the same group also reported a self-injection-locked second-harmonic integrated source with an SHG power of 2 mW through integrating a DFB laser to a PPLN resonator chip.¹⁴³ Additionally, Cheng's group recently reported an electrically pumped compact laser through a hybrid integrated 980-nm band laser diode to an erbium-doped LN microring chip.⁹⁶ In experiments, a single-mode laser operating at 1531.7 nm with a

linewidth of 0.05 nm was observed with a threshold of 6 mW and a conversion efficiency of 3.9×10^{-5} .

3.2 Heterogeneous Integration and Microtransfer Printing III-V Lasers and Amplifiers

Besides hybrid integration, de Beeck et al. reported a novel strategy for the microtransfer printing of III/V gain materials on a thin-film LN platform.³² First, the rib waveguides were fabricated starting from a 500-nm X-cut LN thin film with a sapphire substrate by the EBL-Ar⁺ etching process. To realize the EO phase shifting and lasing wavelength tuning, metal electrodes were introduced on the partially etched LN layer. Then, a 400-nm-thick coupon of crystalline silicon (Si) was microtransfer-printed on the LN recess as an intermediate layer and patterned. Finally, a prefabricated III-V semiconductor optical amplifier was microtransfer-printed on the Si waveguide. The schematic drawing at different cross sections in this platform is shown in the upper part of Fig. 12(a). Based on the heterogeneously integrated semiconductor optical amplifier system, multimode ring lasers and single-mode tunable lasers were investigated by designing a microring resonator structure with a directional coupler and a pair of electro-optically tunable ring resonator mirror structures, respectively, as shown in the bottom of Fig. 12(a).

Experimentally, the gain performance of the III/V-on-LN amplifier was characterized first under different bias currents with a fixed input power of -22.7 dBm. A maximal gain of 11.8 dB

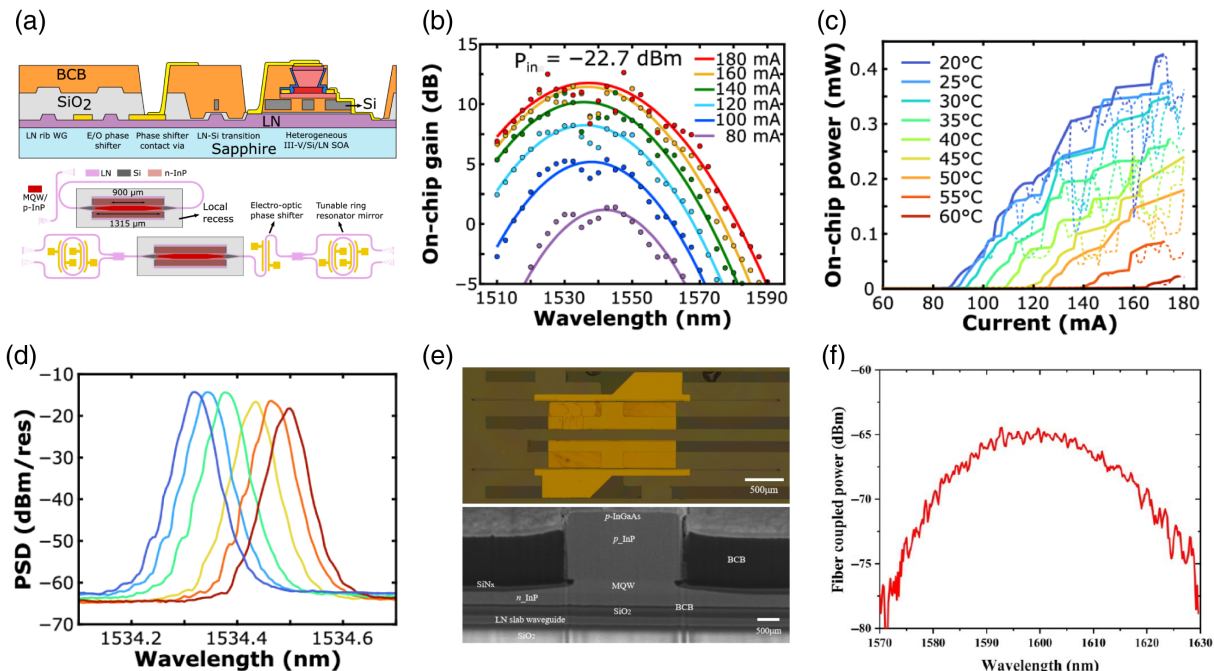


Fig. 12 (a) Top: schematic drawing of the different cross-sections for the heterogeneous integration platform. Bottom: schematic diagram of the designed ring laser and single-mode tunable laser. (b) Measured gain bandwidth of the III/V-on-LN amplifier. (c) Obtained LI curves of the ring laser at different temperatures. (d) Recorded spectra of the fine wavelength tuning of the single-mode laser. (a)–(d) Reprinted from Ref. 32, © 2021 Optica. (e) Optical microscopy image and SEM image of the cross-section of the heterogeneously integrated III-V-on-LN device. (f) Detected electroluminescence spectrum of the heterogeneously integrated III-V-on-LN broadband light sources. (e) and (f) Reprinted from Ref. 144, © 2022 Optica.

was obtained at 1537 nm with a 3-dB gain bandwidth up to 45 nm for a bias current of 180 mA, as shown in Fig. 12(b). Then, the L-I curves of the multimode ring laser at different temperatures were measured, as shown in Fig. 12(c). The laser operating at the temperature range of 20°C to 60°C was investigated, and an output power of 427 μ W was obtained at the temperature of 20°C. Additionally, the phenomenon of laser power oscillation caused by mode hopping was also observed. Afterward, the coarse wavelength tuning of the single-mode tunable laser with a range of 21 nm was observed by applying a voltage to the electrodes of the ring resonator mirror. In addition, a fine-tuning range of 180 pm was realized by changing the bias voltage over the ring mirrors, as shown in Fig. 12(d). Furthermore, an output power of 0.77 mW was detected for the single-mode laser with a fundamental linewidth below 1.5 MHz. Compared with the hybrid integration by butt coupling, the microtransfer printing method could integrate active devices with wafer-scale and electrically pretested active devices on their native substrate, leading to high throughput.

More recently, Zhang et al. demonstrated a heterogeneous integration of III-V active device on LNOI waveguide by adhesive bonding, as shown in Fig. 12(e).¹⁴⁴ An electroluminescence spectrum with a 3-dB bandwidth of 40 nm centered at 1600 nm was observed, as shown in Fig. 12(f). Moreover, due to selecting the InP-based III-V material, the active devices can also function as a photodetector. A peak responsivity of 0.38 A/W at 1540 nm with a low dark current of 9 nA at -0.5 V was detected. The co-integration of a light source and a photodetector enables a fully integrated transceiver based on an LNOI photonics platform.

The electrically pumped lasers and amplifiers have the characteristics of portability, which is more conducive to the application out of the laboratory and can eliminate the influence of doping on non-gain area devices, which is a beneficial supplement to the optically pumped LNOI light sources. Table 3 summarizes the main parameters of LNOI electrically pumped lasers reported so far. Hybrid integration, heterogeneous integration, and microtransfer printing have their advantages and limitations. For example, with the help of commercial mature semiconductor single-frequency lasers or amplifiers and the fabricated

low-loss LNOI devices, as well as the introduction of end-coupler design and fine adjustment and alignment before final packaging, hybrid integrated electrically pumped lasers can obtain narrow linewidth and high output power. The disadvantage is that hybrid integration requires high-precision alignment tools and can only integrate a single device at a time, which increases the cost of integrated devices to some extent and is therefore more suitable for initial prototype exploration. On the other hand, the heterogeneous integration and microtransfer printing technology can realize wafer-scale preparation and effectively lead to high throughput. However, due to the complexity of the preparation process, the whole process is still in the research and development stage. Inconsistent thermal diffusivity and unmatched refractive index of different film layers result in a low yield of products, especially for heterogeneous integrated products. In addition, the microtransfer-printing process is complex and requires high alignment accuracy (<1 μ m), which is challenging to meet the general micro-nano processing platform.¹³⁹ Moreover, the output power of the laser is much lower than that of the flip-chip hybrid integrated laser. It is mainly due to the low coupling efficiency caused by the low alignment accuracy between the gain amplifier and passive component, as well as the fact that the integrated gain component is a III-V amplifier rather than a III-V laser, which limits the available power coupled to the LN layer. A promising way is to transfer the prepared III-V FP cavity device to the silicon-based photon platform with a butt-coupling scheme to improve the output power of the integrated laser.^{145,146} Additionally, the scheme of realizing electrically pumped lasers through heterogeneous integration with wafer bonding technology was reported rarely and there is plenty of room for performance improvement.¹⁴⁷

As can be seen from the above introduction, various lasers and amplifiers based on the LNOI platform have been demonstrated by doping REIs or integrating III-V gain materials. Nevertheless, the two gain introduction schemes have their advantages and disadvantages. Specifically, compared with III-V gain media, REI-doped materials have a long excited-state lifetime and less refractive index change, resulting in relatively higher temperature stability, lower noise figure, and narrower laser linewidth for the REI-doped laser and amplifier. For

Table 3 Typical parameters comparison of reported electrically pumped LNOI lasers.^a

Integrated methods	Working wavelength (nm)	Threshold current (mA)	Output power (mW)	Tuning range (nm)	SMSR (dB)	Linewidth	References
Hybrid integration	1331.88	100	2.5	36.4	60	—	30
Hybrid integration	1558	~60	60	—	~60	1 MHz	33
Hybrid integration	1581.12	80	5.5	20	50	11.3 kHz	34
Microtransfer printing	~1534	~85	0.77	21	~40	<1.5 MHz	32
Hybrid integration	1555.4	—	$\sim 5 \times 10^{-3}$	—	50	3.14 kHz	140
Hybrid integration	1556.3	—	1	—	>60	—	141
Heterogeneous integration	1600	—	$\sim 3.2 \times 10^{-7}$	—	—	—	144
Hybrid integration	1531.7	500	5.8×10^{-4}	—	—	0.05 nm	96
Hybrid integration	1328.3	—	~2	40.3	>60	475 kHz	142
Heterogeneous integration	1590	80	1.3	—	30	—	31

^aAll results are approximate values obtained from the reported literature.

example, 4 Hz of the fundamental linewidth of lasers based on erbium-doped silica microtoroid cavity has been demonstrated.¹⁴⁸ Therefore, lasers and amplifiers based on REI-doped LNOI are more suitable for on-chip coherent communication, quantum optics, and other related applications. Another advantage of the REIs-doped LNOI lasers and amplifiers is that the fabrication process is simple and compatible with the CMOS process, which promises to be scalable, low-cost, and amenable to mass production. But the output power for the REI-doped LNOI lasers and amplifiers is still at a low level (μW -level), which substantially limits the application of nonlinear frequency conversion and soliton comb based on on-chip active light sources. To enhance the output power, the doping concentration and resonator geometry, as well as the resonator size, need to be carefully studied and designed. On the other hand, the electrically pumped lasers based on LNOI through integrating III-V materials have the characteristics of high output power, adjustable broadband, and convenient operation. It can be widely used as an optical transmitter in long-distance communication networks and data center optical interconnection, and other related scenes. However, there are also some shortcomings for electrically pumped LNOI light sources. For example, the external gain chip of the hybrid integration needs to finely adjust the coupling between the active chip and LNOI passive chip before work. Therefore, it is challenging to realize batch preparation, leading to increased costs and preparation period. In addition, the preparation process of the heterogeneous integration scheme is complex, and the microtransfer printing scheme requires high alignment accuracy for the active-passive coupling transition process.

4 Application Prospects of LNOI-Based Lasers and Amplifiers

Based on the realization of the long-awaited active light source, a series of promising applications are expected to be carried out based on the platform of REI-doped LN film. This section discusses the application fields of combining on-chip light sources with other LNOI functional devices, including sensors, electro-optic modulators, frequency converters, and microcavity combs.

4.1 Sensing Based on LNOI Light Sources

WGM microcavity has a high Q value and a small mode volume, which can strongly enhance the interaction between light and matter. It is thus regarded as a high-sensitivity platform in sensing applications.^{149,150} The main detection mechanism of WGM microcavity sensing is to monitor the mode drift, mode broadening, and mode splitting of the microcavity transmission spectrum. Compared with the passive resonator mode, the lasing mode has a narrower linewidth due to its gain, which is beneficial to further improve the sensitivity of detection.¹⁵¹ For example, He et al. realized single virus and nanoparticle detection based on erbium-doped silica WGM microlaser.¹⁵² In addition, the low threshold feature of the WGM laser is of great significance in biosensing applications, where light damage needs to be avoided. Therefore, combined with the excellent photoelectric properties of LN, the REI-doped LNOI microcavity laser is an attractive prospect for sensing applications. In addition, the demonstrated ytterbium-doped LNOI microlasers are expected to detect molecules in liquid solution due to weak water absorption in this band.^{72,73,79}

4.2 Broadband Optical Communication

The optical transmitter is an essential building block in optical communication applications, and its critical component is the modulator module. Electro-optic modulators based on LNOI have been developed and shown noticeable advantages in driving voltage, bandwidth, linearity, and excitation ratio. However, due to the inherent luminescence difficulties of LN materials, the lack of an on-chip integrated light source, especially the electrically pumped high-power light source, is considered the main obstacle for applying the LNOI modulator to the optical transmitter. With the development of LN thin-film lasers, electrically pumped high-power lasers have become possible, effectively overcoming this limitation. In the future, an LN thin-film optical transmitter with low power consumption and high performance is expected to play an important role in data centers. In addition, to further increase the capacity of optical communication, the broadband tunable laser sources realized on the LNOI platform were expected to combine with the on-chip electro-optical modulator and wavelength division multiplexer¹⁵³ for the construction of a multichannel wavelength division multiplexer emitter, which is helpful to achieve ultrabroadband optical fiber communication and reduce the communication costs.

4.3 Frequency Converter Based on LNOI Active Light Source

It can be seen from Tables 1 and 3 that the reported lasers are mainly concentrated in the 1550- and 1060-nm bands. In addition, a single type of REI or semiconductor gain medium has a limited gain bandwidth (~ 100 nm), which limits the application range of gain chips to a certain extent. Fortunately, LN has good second-order nonlinear characteristics, which can effectively expand the bandwidth of light sources. Nonlinear wavelength conversion processes based on LNOI resonators and waveguides, such as SHG, SFG, and differential frequency generation, have been confirmed successfully and have obtained better performance than traditional bulk LN devices.^{154,155} In the future, combined with the excellent second-order nonlinearity of LN, the LNOI active laser can be used to obtain the desired light sources flexibly. For example, the 530-nm band light source can be generated through the cascade second-order nonlinear process of SHG-SFG by combining the C-band LNOI laser and the PPLN structure designed to achieve a phase-matching condition, which effectively alleviates the limitation of the low luminous efficiency of the gain material in the band referred to as the “green gap”.

4.4 Chip-Based Microcombs

Optical frequency combs have attracted wide attention due to their application in optical clocks, metrology, and spectroscopy. Especially in recent years, the optical comb generated in the WGM microresonators, referred to as microcombs, has the excellent characteristics of low power consumption, high repetition rate, and on-chip integration compatibility, which endows the optical frequency comb with a new generation mechanism and application range. The LN has excellent third-order nonlinear and electro-optical effects. The soliton microcomb¹⁹ and broadband electro-optic frequency comb based on the LN platform have been confirmed, which shows the feasibility of the LN thin-film platform to generate an optical microcomb. In addition, based on the unique electro-optic effect of LN, the

generation and modulation of an optical microcomb can be realized simultaneously on a monolithic chip, which can expand the application field of microcombs, such as programmable pulse shaping and coherent microwaves processing.^{156,157} With the development of LN thin-film laser sources, the combination of laser and high-quality Kerr microcavity is a promising way to realize the miniaturization and integration of the microcomb system, which can enhance the portability of the microcomb and expand its application scenarios, such as parallel coherent lidar. Some research routes can refer to the development of a silicon nitride-based integrated optical microcomb. For example, electrically pumped soliton frequency combs are generated by hybrid integrating semiconductor amplifiers or lasers with passive silicon nitride chips.^{158–160} Furthermore, laser soliton microcombs based on a wafer-scale fabrication process are reported by heterogeneously integrated InP semiconductor lasers on an ultralow-loss silicon nitride platform.¹⁶¹ On the other hand, on-chip mode-locked lasers are another way to realize chip-level optical frequency combs. The realization of a mode-locked laser based on the introduction of saturable absorber into chip-based laser has been confirmed on the silicon nitride integrated platform,^{138,162} which can also provide a reference for the research of mode-locked lasers on an LNOI active light source platform. In addition, the multilongitudinal mode laser output based on REI-doped LNOI microcavity is also expected to achieve a mode-locked laser by introducing a saturable absorber or loading active regulation, such as electro-optic modulation to lock each longitudinal mode signal.¹⁶³ In the early stage, the application of the electro-optic effect of LN to realize mode-locked lasers was demonstrated on the erbium-doped LN weak waveguide.¹⁶⁴

5 Conclusion

In this review, the current research progress on lasers and amplifiers based on LN thin-film platforms was reviewed

comprehensively. Specifically, in the section on optical pumping laser and amplifier realized by REI doping, several mainstream ways of introducing REIs into LN were introduced, and their advantages and disadvantages were discussed. Then the fluorescence spectrum research of REIs based on the LNOI platform was introduced. Then, vital parameters of the WGMs microlasers, such as threshold and conversion efficiency, were analyzed. On this basis, the research progress on microdisks, microrings, and single-mode lasers on the REI-doped LNOI platform is introduced. At the same time, the research on the REI-doped LNOI amplifiers was also reviewed. The limitations and improvement measures of the current optically pumped lasers and amplifiers were also discussed. On the other hand, in the section on LNOI electrically pumped III-V lasers and amplifiers, several mainstream mechanisms of introducing III-V gain materials into the current integrated photonics platform, namely, hybrid integration, heterogeneous integration, and microtransfer printing, were introduced in detail. The research progress on LNOI electrically pumped III-V lasers and amplifiers was reviewed. On this basis, the restrictions and improvement schemes for the current realization of electrically pumped lasers and amplifiers were explored in depth. Then the advantages and disadvantages of the two routes to realizing LNOI lasers and amplifiers were also discussed. Finally, the application scenarios based on the combination of an LNOI-based light source and other excellent device-based LN thin-film platforms, such as sensing, frequency conversion, and on-chip optical communication, were envisioned.

In addition to the rapid development of various photoelectric devices of LN thin-film platforms, the realization of on-chip light sources will undoubtedly make the LN thin-film platform achieve a high degree of integration. At the same time, detectors based on Si,¹⁶⁵ black phosphorus,^{166,167} and superconducting nanowires^{168,169} have been proven on the LNOI platform, demonstrating the feasibility of integrated photodetectors. Furthermore, the experience of heterogeneously integrated III-V photodetectors

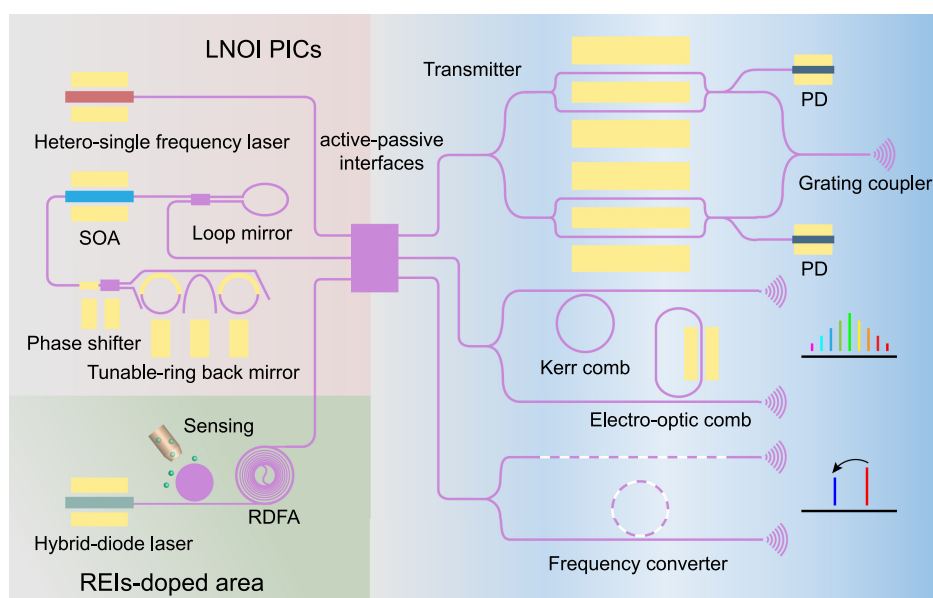


Fig. 13 Schematic diagram of integrated optical chips based on LN thin film. SOA, semiconductor optical amplifier; RDFA, rare-earth-doped waveguide amplifier; PD, photodetector; and SHG, second-harmonic generation.

based on Si-based photonics can also be transferred into the LN thin-film platform and is expected to achieve high detector bandwidth.^{170–172} Figure 13 shows an envisaged schematic diagram of several integrated multifunctional photonic circuits on an LN thin-film platform, including integrated lasers, amplifiers, frequency converters, electro-optic modulators, photodetectors, and other key devices. These integrated photonic chips will benefit the field of optical communication, laser radar, particle sensing, information processing, and so on. In the future, the highly integrated versatile LNOI chips are expected to move out of the laboratory and lead to more practical applications.

Acknowledgments

The authors thank Zhenzhong Hao, Dahuai Zheng, and Yuqi Zhang for their insightful discussions and feedback on this manuscript. This work was financially supported by the National Key Research and Development Program of China (Grant No. 2019YFA0705000); National Natural Science Foundation of China (Grant Nos. 92250302, 12034010, 12134007, 92050111, 12074199, 92050114, and 12004197); and the 111 Project (Grant No. B23045). The authors declare no conflicts of interest.

References

- G. Poberaj et al., “Lithium niobate on insulator (LNOI) for micro-photonics devices,” *Laser Photonics Rev.* **6**, 488 (2012).
- A. Boes et al., “Status and potential of lithium niobate on insulator (LNOI) for photonic integrated circuits,” *Laser Photonics Rev.* **12**(4), 1700256 (2018).
- Y. Qi and Y. Li, “Integrated lithium niobate photonics,” *Nanophotonics* **9**(6), 1287 (2020).
- C. Wang et al., “Integrated high quality factor lithium niobate microdisk resonators,” *Opt. Express* **22**(25), 30924 (2014).
- R. Wu et al., “Lithium niobate micro-disk resonators of quality factors above 10^7 ,” *Opt. Lett.* **43**(17), 4116 (2018).
- J. Wang et al., “High- Q lithium niobate microdisk resonators on a chip for efficient electro-optic modulation,” *Opt. Express* **23**(18), 23072 (2015).
- R. Gao et al., “Lithium niobate microring with ultra-high Q factor above 10^8 ,” *Chin. Opt. Lett.* **20**, 011902 (2022).
- J. Zhang et al., “Fabrication of crystalline microresonators of high quality factors with a controllable wedge angle on lithium niobate on insulator,” *Nanomaterials* **9**(9), 1218 (2019).
- R. Wu et al., “Long low-loss-lithium niobate on insulator waveguides with sub-nanometer surface roughness,” *Nanomaterials* **8**(11), 910 (2018).
- M. Zhang et al., “Monolithic ultra-high- Q lithium niobate microring resonator,” *Optica* **4**(12), 1536 (2017).
- C. Wang et al., “Integrated lithium niobate electro-optic modulators operating at CMOS-compatible voltages,” *Nature* **562**(7725), 101 (2018).
- M. He et al., “High-performance hybrid silicon and lithium niobate Mach-Zehnder modulators for 100 Gbit s⁻¹ and beyond,” *Nat. Photonics* **13**(5), 359 (2019).
- M. Zhang et al., “Integrated lithium niobate electro-optic modulators: when performance meets scalability,” *Optica* **8**(5), 652 (2021).
- M. Xu and X. Cai, “Advances in integrated ultra-wideband electro-optic modulators [Invited],” *Opt. Express* **30**(5), 7253 (2022).
- J. Lin et al., “Broadband quasi-phase-matched harmonic generation in an on-chip monocrystalline lithium niobate microdisk resonator,” *Phys. Rev. Lett.* **122**(17), 173903 (2019).
- J.-Y. Chen et al., “Ultra-efficient frequency conversion in quasi-phase-matched lithium niobate microrings,” *Optica* **6**(9), 1244 (2019).
- J. Lu et al., “Toward 1% single-photon anharmonicity with periodically poled lithium niobate microring resonators,” *Optica* **7**(12), 1654 (2020).
- Z. Hao et al., “Second-harmonic generation using d_{33} in periodically poled lithium niobate microdisk resonators,” *Photonics Res.* **8**(3), 311 (2020).
- Y. He et al., “Self-starting bi-chromatic LiNbO₃ soliton microcomb,” *Optica* **6**(9), 1138 (2019).
- Z. Gong et al., “Near-octave lithium niobate soliton microcomb,” *Optica* **7**(10), 1275 (2020).
- M. Zhang et al., “Broadband electro-optic frequency comb generation in a lithium niobate microring resonator,” *Nature* **568**(7752), 373 (2019).
- D. Zhu et al., “Integrated photonics on thin-film lithium niobate,” *Adv. Opt. Photonics* **13**(2), 242 (2021).
- G. Chen et al., “Advances in lithium niobate photonics: development status and perspectives,” *Adv. Photon.* **4**, 034003 (2022).
- R.-R. Xie et al., “Microresonators in lithium niobate thin films,” *Adv. Opt. Mater.* **9**(19), 2100539 (2021).
- Y. Jia, L. Wang, and F. Chen, “Ion-cut lithium niobate on insulator technology: recent advances and perspectives,” *Appl. Phys. Rev.* **8**(1), 011307 (2021).
- J. Lin et al., “Advances in on-chip photonic devices based on lithium niobate on insulator,” *Photonics Res.* **8**(12), 1910 (2020).
- Y. Liu et al., “On-chip erbium-doped lithium niobate microcavity laser,” *Sci. China-Phys. Mech. Astron.* **64**(3), 234262 (2021).
- R. Zhang et al., “Integrated lithium niobate single-mode lasers by the Vernier effect,” *Sci. China-Phys. Mech. Astron.* **64**(9), 294216 (2021).
- X. Yan et al., “Integrated spiral waveguide amplifiers on erbium-doped thin-film lithium niobate,” arXiv:2105.00214 (2021).
- Y. Han et al., “Electrically pumped widely tunable O-band hybrid lithium niobate/III-V laser,” *Opt. Lett.* **46**(21), 5413 (2021).
- X. Zhang et al., “Heterogeneous integration of III-V semiconductor lasers on thin-film lithium niobate platform by wafer bonding,” *Appl. Phys. Lett.* **122**(8), 081103 (2023).
- C. Op de Beeck et al., “III/V-on-lithium niobate amplifiers and lasers,” *Optica* **8**(10), 1288 (2021).
- A. Shams-Ansari et al., “Electrically pumped laser transmitter integrated on thin-film lithium niobate,” *Optica* **9**(4), 408 (2022).
- M. Li et al., “Integrated Pockels laser,” *Nat. Commun.* **13**(1), 5344 (2022).
- E. Lallier, “Rare-earth-doped glass and LiNbO₃ waveguide lasers and optical amplifiers,” *Appl. Opt.* **31**(25), 5276 (1992).
- E. Cantelar et al., “Modelling of optical amplification in Er/Yb co-doped LiNbO₃ waveguides,” *Opt. Quantum. Electron.* **32**(6/8), 819 (2000).
- W. Sohler et al., “Erbium-doped lithium niobate waveguide lasers,” *IEICE Trans. Electron.* **E88C**(5), 990 (2005).
- M. George et al., “In-band pumped Ti:TM:LiNbO₃ waveguide amplifier and low threshold laser,” *Laser Photonics Rev.* **7**(1), 122 (2013).
- P. Izabella et al., “Single crystal growth and optical properties of LiNbO₃ doped with Er³⁺, Tm³⁺ and Mg²⁺,” *Proc. SPIE* **2373**, 65 (1995).
- M. N. Palatnikov et al., “Growth and concentration dependencies of rare-earth doped lithium niobate single crystals,” *J. Cryst. Growth* **291**(2), 390 (2006).
- I. Baumann et al., “Erbium incorporation in LiNbO₃ by diffusion-doping,” *Appl. Phys. A* **64**(1), 33 (1996).
- M. Fleuster et al., “Optical and structural properties of MeV erbium-implanted LiNbO₃,” *J. Appl. Phys.* **75**(1), 173 (1994).
- P. Becker et al., “Er-diffused Ti:LiNbO₃ waveguide laser of 1563 and 1576 nm emission wavelengths,” *Appl. Phys. Lett.* **61**(11), 1257 (1992).

44. A. Polman, "Erbium implanted thin film photonic materials," *J. Appl. Phys.* **82**(1), 1 (1997).
45. Y. Jia et al., "Integrated photonics based on rare-earth ion-doped thin-film lithium niobate," *Laser Photonics Rev.* **16**(9), 2200059 (2022).
46. Y. Chen, "Photonic integration on rare earth ion-doped thin-film lithium niobate," *Sci. China-Phys. Mech. Astron.* **65**(9), 294231 (2022).
47. S. Dutta et al., "Integrated photonic platform for rare-earth ions in thin film lithium niobate," *Nano Lett.* **20**(1), 741 (2020).
48. S. Wang et al., "Incorporation of erbium ions into thin-film lithium niobate integrated photonics," *Appl. Phys. Lett.* **116**(15), 151103 (2020).
49. D. Pak et al., "Ytterbium-implanted photonic resonators based on thin film lithium niobate," *J. Appl. Phys.* **128**(8), 084302 (2020).
50. K. Xia et al., "Tunable microcavities coupled to rare-earth quantum emitters," *Optica* **9**(4), 445 (2022).
51. L. Yang et al., "Photonic integration of $\text{Er}^{3+}:\text{Y}_2\text{SiO}_5$ with thin-film lithium niobate by flip chip bonding," *Opt. Express* **29**(10), 15497 (2021).
52. X. Jiang et al., "Rare earth-implanted lithium niobate: properties and on-chip integration," *Appl. Phys. Lett.* **115**(7), 071104 (2019).
53. S. Dutta et al., "An atomic frequency comb memory in rare-earth doped thin-film lithium niobate," arXiv:2111.01942 (2021).
54. S. Wang et al., "Er:LiNbO₃ with high optical coherence enabling optical thickness control," *Phys. Rev. A* **18**(1), 014069 (2022).
55. C. W. Thiel, T. Böttger, and R. L. Cone, "Rare-earth-doped materials for applications in quantum information storage and signal processing," *J. Lumin.* **131**(3), 353 (2011).
56. T. Böttger et al., "Optical decoherence and spectral diffusion at 1.5 μm in $\text{Er}^{3+}:\text{Y}_2\text{SiO}_5$ versus magnetic field, temperature, and Er^{3+} concentration," *Phys. Rev. B* **73**(7), 075101 (2006).
57. C. E. Rüter et al., "Optical characterization of a neodymium-doped lithium-niobate-on-insulator (LNIO)," *Opt. Mater. Express* **11**(12), 4007 (2021).
58. E. M. Purcell, H. C. Torrey, and R. V. Pound, "Resonance absorption by nuclear magnetic moments in a solid," *Phys. Rev.* **69**, 37 (1946).
59. D. J. Heinzen et al., "Enhanced and inhibited visible spontaneous emission by atoms in a confocal resonator," *Phys. Rev. Lett.* **58**(13), 1320 (1987).
60. J. M. Gérard et al., "Enhanced spontaneous emission by quantum boxes in a monolithic optical microcavity," *Phys. Rev. Lett.* **81**(5), 1110 (1998).
61. Q. Xu et al., " Er^{3+} -doped lithium niobate thin film: a material platform for ultracompact, highly efficient active microphotonic devices," *Adv. Photonics Res.* **2**(12), 2100081 (2021).
62. K. J. Vahala, "Optical microcavities," *Nature* **424**(6950), 839 (2003).
63. L. He, Ş. K. Özdemir, and L. Yang, "Whispering gallery microcavity lasers," *Laser Photonics Rev.* **7**(1), 60 (2013).
64. Q. Song, "Microdisk lasers: fundamental physics and practical applications," in *Ultra-High-Q Optical Microcavities*, Y.-F. Xiao et al., Eds., p. 233, World Scientific (2020).
65. L. Yang et al., "Erbium-doped and Raman microlasers on a silicon chip fabricated by the sol-gel process," *Appl. Phys. Lett.* **86**(9), 091114 (2005).
66. S. J. Herr, K. Buse, and I. Breunig, "LED-pumped whispering-gallery laser," *Photonics Res.* **5**(6), B34 (2017).
67. R. Gao et al., "Broadband highly efficient nonlinear optical processes in on-chip integrated lithium niobate microdisk resonators of Q -factor above 10^8 ," *New J. Phys.* **23**(12), 123027 (2021).
68. E. S. Hosseini et al., "Systematic design and fabrication of high- Q single-mode pulley-coupled planar silicon nitride microdisk resonators at visible wavelengths," *Opt. Express* **18**(3), 2127 (2010).
69. C. J. McKinstrie, T. J. Stirling, and A. S. Helmy, "Laser linewidths: tutorial," *J. Opt. Soc. Am. B* **38**(12), 3837 (2021).
70. Z. Wang et al., "On-chip tunable microdisk laser fabricated on Er^{3+} -doped lithium niobate on insulator," *Opt. Lett.* **46**(2), 380 (2021).
71. Q. Luo et al., "Microdisk lasers on an erbium-doped lithium-niobate chip," *Sci. China-Phys. Mech. Astron.* **64**(3), 234263 (2021).
72. Y. Zhou et al., "On-chip microdisk laser on Yb^{3+} -doped thin-film lithium niobate," *Opt. Lett.* **46**(22), 5651 (2021).
73. Q. Luo et al., "On-chip ytterbium-doped lithium niobate micro-disk lasers with high conversion efficiency," *Opt. Lett.* **47**(4), 854 (2022).
74. C. Strohhofer and A. Polman, "Absorption and emission spectroscopy in $\text{Er}^{3+} - \text{Yb}^{3+}$ doped aluminum oxide waveguides," *Opt. Mater.* **21**(4), 705 (2003).
75. S. D. Jackson, "Towards high-power mid-infrared emission from a fibre laser," *Nat. Photonics* **6**(7), 423 (2012).
76. S. Balaji, A. D. Sontakke, and K. Annapurna, " Yb^{3+} ion concentration effects on $\sim 1 \mu\text{m}$ emission in tellurite glass," *J. Opt. Soc. Am. B* **29**(7), 1569 (2012).
77. Q. Luo et al., "On-chip erbium-doped lithium niobate microring lasers," *Opt. Lett.* **46**(13), 3275 (2021).
78. D. Yin et al., "Electro-optically tunable microring laser monolithically integrated on lithium niobate on insulator," *Opt. Lett.* **46**(9), 2127 (2021).
79. Q. Luo et al., "Integrated ytterbium-doped lithium niobate microring lasers," *Opt. Lett.* **47**(6), 1427 (2022).
80. R. Gao et al., "On-chip ultra-narrow-linewidth single-mode microlaser on lithium niobate on insulator," *Opt. Lett.* **46**(13), 3131 (2021).
81. X. Liu et al., "Tunable single-mode laser on thin film lithium niobate," *Opt. Lett.* **46**(21), 5505 (2021).
82. Z. Xiao et al., "Single-frequency integrated laser on erbium-doped lithium niobate on insulator," *Opt. Lett.* **46**(17), 4128 (2021).
83. T. Li et al., "A single-frequency single-resonator laser on erbium-doped lithium niobate on insulator," *APL Photonics* **6**(10), 101301 (2021).
84. J. Lin et al., "Electro-optic tuning of a single-frequency ultranarrow linewidth microdisk laser," *Adv. Photon.* **4**, 036001 (2022).
85. Y. Liang et al., "Monolithic single-frequency microring laser on an erbium-doped thin film lithium niobate fabricated by a photolithography assisted chemo-mechanical etching," *Opt. Contin.* **1**(5), 1193 (2022).
86. Y. Zhu et al., "Electro-optically tunable microdisk laser on Er^{3+} -doped lithium niobate thin film," *Chin. Opt. Lett.* **20**, 011303 (2022).
87. J. Guan et al., "Monolithically integrated high-power narrow-bandwidth microdisk laser," arXiv:2212.10892 (2022).
88. S. Yu et al., "On-chip single-mode thin film lithium niobate laser based on Sagnac loop reflectors," arXiv:2212.12698 (2022).
89. E. H. Bernhardt et al., "Ultra-narrow-linewidth, single-frequency distributed feedback waveguide laser in $\text{Al}_2\text{O}_3:\text{Er}^{3+}$ on silicon," *Opt. Lett.* **35**(14), 2394 (2010).
90. E. S. Hosseini et al., "CMOS-compatible 75 mW erbium-doped distributed feedback laser," *Opt. Lett.* **39**(11), 3106 (2014).
91. M. Pollnau and J. D. B. Bradley, "Optically pumped rare-earth-doped Al_2O_3 distributed-feedback lasers on silicon [Invited]," *Opt. Express* **26**(18), 24164 (2018).
92. D. J. Richardson, J. Nilsson, and W. A. Clarkson, "High power fiber lasers: current status and future perspectives [Invited]," *J. Opt. Soc. Am. B* **27**(11), B63 (2010).
93. C. Jauregui, J. Limpert, and A. Tünnermann, "High-power fibre lasers," *Nat. Photonics* **7**(11), 861 (2013).
94. D. Y. Shen, J. K. Sahu, and W. A. Clarkson, "Highly efficient Er,Yb-doped fiber laser with 188 W free-running and >100 W tunable output power," *Opt. Express* **13**(13), 4916 (2005).
95. Y. Jeong et al., "Erbium:ytterbium codoped large-core fiber laser with 297-W continuous-wave output power," *IEEE J. Sel. Top. Quant. Electron.* **13**(3), 573 (2007).

96. J. Zhou et al., "Laser diode-pumped compact hybrid lithium niobate microring laser," *Opt. Lett.* **47**(21), 5599 (2022).
97. M. A. Tran et al., "Extending the spectrum of fully integrated photonics to submicrometre wavelengths," *Nature* **610**(7930), 54 (2022).
98. Y. Zhou et al., "Monolithically integrated active passive waveguide array fabricated on thin film lithium niobate using a single continuous photolithography process," *Laser Photonics Rev.* **17**(4), 2200686 (2023).
99. H. C. Frankis et al., "Erbium-doped TeO₂-coated Si₃N₄ waveguide amplifiers with 5 dB net gain," *Photonics Res.* **8**(2), 127 (2020).
100. W. A. P. M. Hendriks et al., "Rare-earth ion doped Al₂O₃ for active integrated photonics," *Adv. Phys.: X* **6**, 1833753 (2021).
101. J. D. B. Bradley and E. S. Hosseini, "Monolithic erbium- and ytterbium-doped microring lasers on silicon chips," *Opt. Express* **22**(10), 12226 (2014).
102. K. Mirabbas Kiani et al., "Lasing in a hybrid rare-earth silicon microdisk," *Laser Photonics Rev.* **16**(1), 2100348 (2022).
103. L. Chang et al., "Thin film wavelength converters for photonic integrated circuits," *Optica* **3**(5), 531 (2016).
104. X. Han et al., "Mode and polarization-division multiplexing based on silicon nitride loaded lithium niobate on insulator platform," *Laser Photonics Rev.* **16**(1), 2100529 (2022).
105. R. Wang et al., "Widely tunable 2.3 μm III-V-on-silicon Vernier lasers for broadband spectroscopic sensing," *Photonics Res.* **6**(9), 858 (2018).
106. L. Feng, R. El-Ganainy, and L. Ge, "Non-Hermitian photonics based on parity-time symmetry," *Nat. Photonics* **11**(12), 752 (2017).
107. R. El-Ganainy et al., "Non-Hermitian physics and PT symmetry," *Nat. Phys.* **14**(1), 11 (2018).
108. J. Rönn et al., "Ultra-high on-chip optical gain in erbium-based hybrid slot waveguides," *Nat. Commun.* **10**(1), 432 (2019).
109. S. A. Vázquez-Córdova et al., "Erbium-doped spiral amplifiers with 20 dB of net gain on silicon," *Opt. Express* **22**(21), 25993 (2014).
110. J. D. B. Bradley and M. Pollnau, "Erbium-doped integrated waveguide amplifiers and lasers," *Laser Photonics Rev.* **5**(3), 368 (2011).
111. J. Zhou et al., "On-chip integrated waveguide amplifiers on erbium-doped thin-film lithium niobate on insulator," *Laser Photonics Rev.* **15**(8), 2100030 (2021).
112. Z. Chen et al., "Efficient erbium-doped thin-film lithium niobate waveguide amplifiers," *Opt. Lett.* **46**(5), 1161 (2021).
113. Q. Luo et al., "On-chip erbium-doped lithium niobate waveguide amplifiers [Invited]," *Chin. Opt. Lett.* **19**, 060008 (2021).
114. Y. Liang et al., "A high-gain cladded waveguide amplifier on erbium doped thin-film lithium niobate fabricated using photolithography assisted chemo-mechanical etching," *Nanophotonics* **11**(5), 1033 (2022).
115. Z. Zhang et al., "On-chip integrated Yb³⁺-doped waveguide amplifiers on thin film lithium niobate," *Micromachines* **13**, 865 (2022).
116. Y. Jia et al., "Dual-color upconversion luminescence emission from Er:LiNbO₃ on-chip ridge waveguides," *Results Phys.* **27**, 104526 (2021).
117. M. Cai et al., "Erbium-doped lithium niobate thin film waveguide amplifier with 16 dB internal net gain," *IEEE J. Sel Top. Quantum Electron.* **28**(3), 8200608 (2022).
118. C. Huang and L. McCaughan, "980-nm-pumped Er-doped LiNbO₃ waveguide amplifiers: a comparison with 1484-nm pumping," *IEEE J. Sel Top. Quantum Electron.* **2**(2), 367 (1996).
119. Z. Xiao et al., "Single-frequency dual-cavity laser on erbium-doped lithium niobate on insulator," in *Asia Commun. and Photonics Conf. 2021, Technical Digest Series*, p. T11.4 (2021).
120. J. Kim, "Chip-scale power booster for light," *Science* **376**(6599), 1269 (2022).
121. Y. Liu et al., "A photonic integrated circuit-based erbium-doped amplifier," *Science* **376**(6599), 1309 (2022).
122. F. D. Patel et al., "A compact high-performance optical waveguide amplifier," *IEEE Photonics Technol. Lett.* **16**(12), 2607 (2004).
123. H. Chen, M. Leblanc, and G. W. Schinn, "Gain enhanced L-band optical fiber amplifiers and tunable fiber lasers with erbium-doped fibers," *Opt. Commun.* **216**, 119 (2003).
124. Y. W. Lee et al., "Experimental characterization of a dynamically gain-flattened erbium-doped fiber amplifier," *IEEE Photonics Technol. Lett.* **8**(12), 1612 (1996).
125. Y. Seok Hyun et al., "Dynamic erbium-doped fiber amplifier based on active gain flattening with fiber acousto-optic tunable filters," *IEEE Photonics Technol. Lett.* **11**(10), 1229 (1999).
126. P. F. Wysocki et al., "Broad-band erbium-doped fiber amplifier flattened beyond 40 nm using long-period grating filter," *IEEE Photonics Technol. Lett.* **9**(10), 1343 (1997).
127. L. Yi Bin et al., "A 105-nm ultrawide-band gain-flattened amplifier combining C- and L-band dual-core EDFAs in a parallel configuration," *IEEE Photonics Technol. Lett.* **16**, 1640 (2004).
128. Z. Chen et al., "On-chip waveguide amplifiers for multi-band optical communications: a review and challenge," *J. Lightwave Technol.* **40**(11), 3364 (2022).
129. J. Zhang et al., "III-V-on-Si photonic integrated circuits realized using micro-transfer-printing," *APL Photonics* **4**(11), 110803 (2019).
130. C. Xiang, W. Jin, and J. E. Bowers, "Silicon nitride passive and active photonic integrated circuits: trends and prospects," *Photonics Res.* **10**(6), A82 (2022).
131. N. Li et al., "Integrated lasers on silicon at communication wavelength: a progress review," *Adv. Opt. Mater.* **10**(23), 2201008 (2022).
132. Y. Han et al., "Recent advances in light sources on silicon," *Adv. Opt. Photonics* **14**(3), 404 (2022).
133. C. Yang et al., "Advances in silicon-based, integrated tunable semiconductor lasers," *Nanophotonics* **12**, 197–217 (2023).
134. Z. Zhou et al., "Prospects and applications of on-chip lasers," *eLight* **3**(1), 1 (2023).
135. B. Stern et al., "Compact narrow-linewidth integrated laser based on a low-loss silicon nitride ring resonator," *Opt. Lett.* **42**(21), 4541 (2017).
136. A. Moscoso-Mártir et al., "Hybrid silicon photonics flip-chip laser integration with vertical self-alignment," in *Conf. Lasers and Electro-Opt. Pac. Rim*, p. s2069 (2017).
137. C. Xiang et al., "Narrow-linewidth III-V/Si/Si₃N₄ laser using multilayer heterogeneous integration," *Optica* **7**(1), 20 (2020).
138. S. Cuyvers et al., "Low noise heterogeneous III-V-on-silicon-nitride mode-locked comb laser," *Laser Photonics Rev.* **15**(8), 2000485 (2021).
139. C. Op de Beeck et al., "Heterogeneous III-V on silicon nitride amplifiers and lasers via microtransfer printing," *Optica* **7**(5), 386 (2020).
140. V. Snigirev et al., "Ultrafast tunable lasers using lithium niobate integrated photonics," *Nature* **615**(7952), 411 (2023).
141. Z. Li et al., "Tightly confining lithium niobate photonic integrated circuits and lasers," arXiv:2208.05556 (2022).
142. Y. Han et al., "Widely tunable O-band lithium niobate/III-V transmitter," *Opt. Express* **30**(20), 35478 (2022).
143. J. Ling et al., "Self-injection-locked second-harmonic integrated source," arXiv:2207.03071 (2022).
144. X. Zhang et al., "Heterogeneously integrated III-V-on-lithium niobate broadband light sources and photodetectors," *Opt. Lett.* **47**(17), 4564 (2022).
145. J. Justice et al., "Wafer-scale integration of group III-V lasers on silicon using transfer printing of epitaxial layers," *Nat. Photonics* **6**(9), 610 (2012).

146. J. Juvert et al., "Integration of etched facet, electrically pumped, C-band Fabry-Perot lasers on a silicon photonic integrated circuit by transfer printing," *Opt. Express* **26**(17), 21443 (2018).
147. C. Xiang et al., "High-performance silicon photonics using heterogeneous integration," *IEEE J. Sel Top. Quantum Electron.* **28**(3), 8200515 (2022).
148. L. Yang et al., "A 4-Hz fundamental linewidth on-chip micro-laser," in *Conf. Lasers and Electro-Opt./Quantum Electron. and Laser Sci. Conf. and Photonic Appl. Syst. Technol., OSA Technical Digest Series*, p. CMR2 (2007).
149. N. Toropov et al., "Review of biosensing with whispering-gallery mode lasers," *Light: Sci. Appl.* **10**(1), 42 (2021).
150. X. Jiang et al., "Whispering-gallery sensors," *Matter* **3**(2), 371 (2020).
151. Y. Jun and L. J. Guo, "Optical sensors based on active micro-cavities," *IEEE J. Sel Top. Quantum Electron.* **12**(1), 143 (2006).
152. L. He et al., "Detecting single viruses and nanoparticles using whispering gallery microlasers," *Nat. Nanotechnol.* **6**(7), 428 (2011).
153. Y. Yu et al., "Wavelength-division multiplexing on an etchless lithium niobate integrated platform," *ACS Photonics* **9**(10), 3253 (2022).
154. Y. Zheng and X. Chen, "Nonlinear wave mixing in lithium niobate thin film," *Adv. Phys.: X* **6**, 1889402 (2021).
155. M. G. Vazimali and S. Fathpour, "Applications of thin-film lithium niobate in nonlinear integrated photonics," *Adv. Photon.* **4**, 034001 (2022).
156. C. Wang et al., "Monolithic lithium niobate photonic circuits for Kerr frequency comb generation and modulation," *Nat. Commun.* **10**(1), 978 (2019).
157. Y. He et al., "High-speed tunable microwave-rate soliton microcomb," arXiv:2208.08046 (2022).
158. A. S. Raja et al., "Electrically pumped photonic integrated soliton microcomb," *Nat. Commun.* **10**(1), 680 (2019).
159. B. Stern et al., "Battery-operated integrated frequency comb generator," *Nature* **562**(7727), 401 (2018).
160. B. Shen et al., "Integrated turnkey soliton microcombs," *Nature* **582**(7812), 365 (2020).
161. C. Xiang et al., "Laser soliton microcombs heterogeneously integrated on silicon," *Science* **373**(6550), 99 (2021).
162. E. Vissers et al., "Hybrid integrated mode-locked laser diodes with a silicon nitride extended cavity," *Opt. Express* **29**(10), 15013 (2021).
163. T. S. L. P. Suzuki et al., "Design of a passively mode-locking whispering-gallery-mode microlaser," *J. Opt. Soc. Am. B* **38**(10), 3172 (2021).
164. H. Suche et al., "Modelocked Er:Ti:LiNbO₃-waveguide laser," *Electron. Lett.* **29**(12), 1111 (1993).
165. B. Desiatov and M. Lončar, "Silicon photodetector for integrated lithium niobate photonics," *Appl. Phys. Lett.* **115**(12), 121108 (2019).
166. Y. Xue et al., "Waveguide integrated high-speed black phosphorus photodetector on a thin film lithium niobate platform," *Opt. Mater. Express* **13**(1), 272 (2023).
167. S. Wang et al., "Integration of black phosphorus photoconductors with lithium niobate on insulator photonics," *Adv. Opt. Mater.* **11**(2), 2201688 (2023).
168. A. A. Sayem et al., "Lithium-niobate-on-insulator waveguide-integrated superconducting nanowire single-photon detectors," *Appl. Phys. Lett.* **116**(15), 151102 (2020).
169. R. Cheng et al., "A 100-pixel photon-number-resolving detector unveiling photon statistics," *Nat. Photonics* **17**(1), 112 (2023).
170. A. W. Fang et al., "Integrated AlGaInAs-silicon evanescent race-track laser and photodetector," *Opt. Express* **15**(5), 2315 (2007).
171. J. Brouckaert et al., "Thin-film III-V photodetectors integrated on silicon-on-insulator photonic ICs," *J. Lightwave Technol.* **25**(4), 1053 (2007).
172. J. Wun, Y. Wang, and J. Shi, "Ultrafast uni-traveling carrier photodiodes with GaAs_{0.5}Sb_{0.5}/In_{0.53}Ga_{0.47}As type-II hybrid absorbers for high-power operation at THz frequencies," *IEEE J. Sel Top. Quantum Electron.* **24**(2), 8500207 (2018).

Qiang Luo received his BS degree from Shangqiu Normal University in 2017. Currently, he is a PhD student at TEDA Institute of Applied Physics, Nankai University. His research interests include microlasers and amplifiers based on lithium niobate thin-film platforms.

Fang Bo received his BS (also BE) and PhD degrees from Nankai University in 2002 and 2007, respectively. Currently, he is working as a professor at Nankai University. From 2013 to 2014, he was working as a visiting scholar at Washington University in St. Louis. His research interests include micro/nano-optics, quantum optics, and nonlinear optics, in particular, fabrication and nonlinear effects of on-chip lithium niobate resonators.

Yongfa Kong received his BS and MS degrees from Nankai University and PhD degree from the School of Material Science and Engineering of Tianjin University. Currently, he is working as a professor of physics at Nankai University in China. He has worked at the School of Physics of Nankai University since 1999 following postdoctoral appointments at the Photonics Center of Nankai University. His research interests are diverse and cover the physics and devices of nonlinear optical and photonic materials.

Guoquan Zhang received his bachelor's degree in 1993, the master's degree in 1995 in condensed matter physics, and the PhD in condensed matter physics from Nankai University, Tianjin, China. Currently, he is working as a professor at Nankai University. His research interests include nonlinear optics and quantum optics.

Jingjun Xu received his BS degree in solid-state physics and PhD in condensed matter physics from Nankai University in 1988 and 1993, respectively. Currently, he is working as a professor at the School of Physics at Nankai University. He is the founding director of the Ministry of Education Key Laboratory of Weak-Light Nonlinear Photonics. His research interests include nonlinear photonic materials and physics and their application in information technology.